Nano Research 2017, 10(5): 1471–1497
DOI 10.1007/s12274-016-1405-2
Review Article
ISSN 1998-0124
CN 11-5974/O4

Tailoring interface of lead-halide perovskite solar cells

Peimei Da and Gengfeng Zheng (✉)

Laboratory of Advanced Materials, Department of Chemistry, Collaborative Innovation Center of Chemistry for Energy Materials, Fudan University, Shanghai 200438, China

Received: 25 October 2016
Revised: 3 December 2016
Accepted: 4 December 2016

KEYWORDS
perovskite solar cell, interface engineering

ABSTRACT

Lead-halide perovskite solar cells (PSCs) have attracted tremendous attention during the past few years owing to their extraordinary electronic and photonic properties. To improve the performances of PSCs, many researchers have focused on the compositional engineering, solvent engineering, and film fabrication methodologies. Interfacial engineering of PSCs has become a burgeoning field in which researchers aim to deeply understand the mechanisms of cells and thereby increase the efficiency and stability of PSCs. This review focuses on the interface tailoring of lead-halide PSCs, including the modification of each layer of the cell structure (i.e., perovskite absorber, electron-transport layers, and hole-transport layers) and the interfacial materials that can be introduced into the PSCs.

1 Introduction

The rapid development of hybrid organic–inorganic perovskite solar cells (PSCs) has attracted tremendous interest among scientific communities concerned with worldwide shortages of energy supplies. The general chemical formula of perovskite materials originates from calcium titanium oxide ABX_3, where A is a large organic cation (typically $CH_3NH_3^+$, $HC(NH_2)_2^+$), B is a metal cation (typically Pb^{2+}), and X is a halide (I^-, Br^-, Cl^-). In just the last few years, the power-conversion efficiency (PCE) of PSCs has drastically increased from the value of 3.81% [1] reported by Miyasaka and co-workers to a recently certified PCE of 22.1%, according to the latest research-cell efficiencies recorded by the National Renewable Energy Laboratory [2]. This efficiency rivals those of other thin-film technologies in the photovoltaic community, such as CdTe and copper indium gallium (di)selenide (CIGS). The dazzling performance of the organic–inorganic hybrid perovskite is attributed to its ambipolar charge carrier transport property, large carrier diffusion length, large absorption coefficient, and tunable direct bandgap [3]. The efficiency limit of $CH_3NH_3PbI_3$ PSCs without angular restriction is estimated to be 31% [4], which means that the current performance of PSCs is still far below its ceiling.

Along with the application of appropriate materials, the high quality of each layer and an optimized cell structure, interface-related charge generation, and the

Address correspondence to gfzheng@fudan.edu.cn

charge collection and transport efficiencies are of vital importance for PSCs. The photoinduced charge carriers must move across several interfaces to be collected; thus, the interfacial defects, energy-level alignment, and charge distribution significantly impact the final performance of PSCs. Furthermore, the notorious stability problems of PSCs are directly related to the interfaces. Fan et al. recently reviewed studies on the degradation mechanisms of organometallic trihalide PSCs and proposed strategies for stability improvement [5]. A decrease in the PCE is associated with the chemical degradation of the metal contact due to ionic movement in the perovskite layer [6]. With regard to these issues, the present review mainly focuses on the progress of interfacial engineering in lead-iodide PSCs, including interface optimization caused by modification of the perovskite absorber, electron-transport layer (ETL), hole-transport layer (HTL), and materials applied as introduced interfacial layers in the PSCs.

2 Interfaces in PSCs

PSCs have been proven to be free carrier-based devices [7–9] in which charge transport and separation occur as in heterojunction solar cells [10]. According to the Anderson model and thermal equilibrium theory [11], when two types of semiconductors contact directly, the free carriers in the semiconductors diffuse towards each other spontaneously. This diffusion unifies the Femi energy level and yields a charge-depletion region with a built-in electric field, which is defined as a junction. A smooth energy band bending can be obtained in a p–n junction; however, an energy cliff always appears at the interface of the heterojunction. This is due to band offset [12], which significantly influences the voltage output of a PSC. The interfacial electronic and energy structures can also directly affect the charge extraction and collection, as revealed by experiments and theoretical calculations [13–16]. However, more rigorous work is required to fully understand the complicated device system.

As shown in Fig. 1, a typical PSC, regardless of whether it has a mesoscopic nanostructured solar cell, planar heterojunction (n–i–p), or inverted planar heterojunction (p–i–n) cell structure, is composed of a

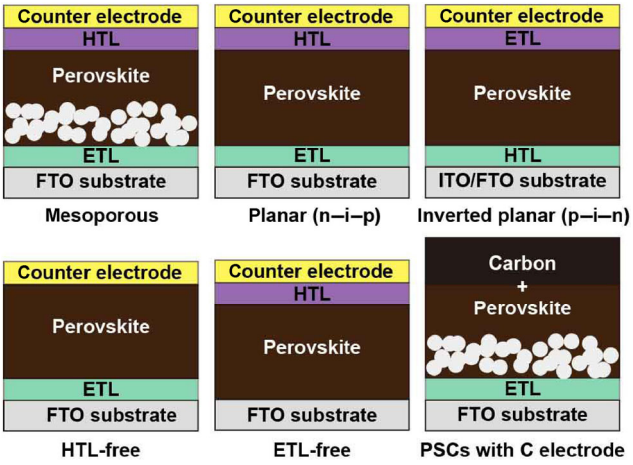

Figure 1 Several typical structures of PSCs.

transparent substrate (e.g., fluorine-doped or indium-doped tin oxide, FTO or ITO, respectively), a perovskite absorber layer sandwiched between the ETL and HTL, and a metal counter electrode on top. For conventional structured PSCs (mesoscopic and n–i–p), illumination is applied to the ETL beforehand, and for inverted planar heterojunction structures, illumination is applied to the HTL beforehand. Thus, for the mesoscopic and planar heterojunction cell structure, the interfaces in PSCs are mainly substrate/ETL, ETL/perovskite, perovskite/HTL, and HTL/counter electrode, and for inverted planar heterojunction solar cells, they are substrate/HTL, HTL/perovskite, perovskite/ETL, and ETL/counter electrode.

Most reported high-efficiency PSCs use noble metal such as Au or Ag as the counter electrode, which are usually prepared by high-vacuum thermal or e-beam evaporation or sputtering. Recently, earth-abundant and cheaper metals such as Al, Ni [17], Mo [18], and AgAl alloys [19] have also been successfully applied in PSCs. Fan et al. reported an inspiring application of a mesoporous Ni counter electrode for printable and reusable PSCs [20]. The effects of the ETL and HTL on the metal-electrode work function have been simulated, and the threshold value of the metal-electrode work function for 2,2′,7,7′-tetrakis[N,N-di(4-methoxyphenyl)-amino]-9,9′-spirobifluorenre (spiro-OMeTAD), NiO, CuI, and Cu_2O were calculated to be 4.9, 4.8, 4.7, and 4.9 eV, respectively [21], providing helpful guidelines for the selection of materials and metal electrodes for PSCs. Carbon materials are very promising candidates for counter electrodes in PSCs

owing to their low cost, good chemical stability, suitable energy levels, and easy fabrication. Several groups have reported successful application and comparable efficiency of PSCs with carbon electrodes [22–24]. Among these, Han's group was the first to report the implementation of a carbon counter electrode in $CH_3NH_3PbI_3$-based solar cells [25]. PSCs with HTL-free [24, 25] and ETL-free [26, 27] solar cells have also been reported, mainly for cheaper and potentially large-scale industrial production.

Upon illumination, when photons are absorbed by the perovskite absorber, free electrons and holes are excited. The free carriers must first travel in the perovskite absorber by migration or diffusion, during this process the carriers might recombine or be scattered because of crystal boundaries and defects. Then, electrons and holes are extracted by the ETL and HTL, respectively. For a high PCE, all the photoinduced carriers are expected to reach the external load. However, defects due to lattice mismatch, inappropriate energy-level alignment, uncoordinated electrons, and thermal vibrations always exist in interfaces [12, 13]. The ETL prevents the holes generated in perovskite absorber from reaching the cathode, which is also referred to as the hole-blocking layer. If the lowest unoccupied molecular orbital (LUMO) of the ETL is far lower than that of the absorber, the open-circuit voltage (V_{oc}) decreases. Similarly, the highest occupied molecular orbital (HOMO) of the HTL must be only slightly higher than that of the absorber to extract holes and block electrons efficiently. Moreover, serious recombination can be caused by the accumulation of free carriers at the notches between interfaces [12]. It is concluded that the ETL/perovskite interface plays a crucial role in determining V_{oc}, while the perovskite/HTL interface is more dominant in governing the photocurrent. The energy levels of commonly used materials in lead-halide PSCs are illustrated in Fig. 2. TiO_2 and spiro-OMeTAD are most widely adopted as ETLs and HTLs in conventional structured PSCs, while poly(3,4-ethylenedioxythiophene) polystyrene sulfonate (PEDOT:PSS)/NiO_x and [6,6]-phenyl-C_{61}-butyric acid methyl ester (PCBM) are the most widely deployed HTLs and ETLs in inverted planar PSCs. The work functions of adjacent layers in PSCs, which should match well, can be effectively tailored by interface engineering.

Thus far, it is well-recognized that interface engineering is an efficient way to achieve better energy-level alignment, passivate traps in perovskites, eliminate photocurrent hysteresis, retard charge recombination, and enhance the long-term stability of devices.

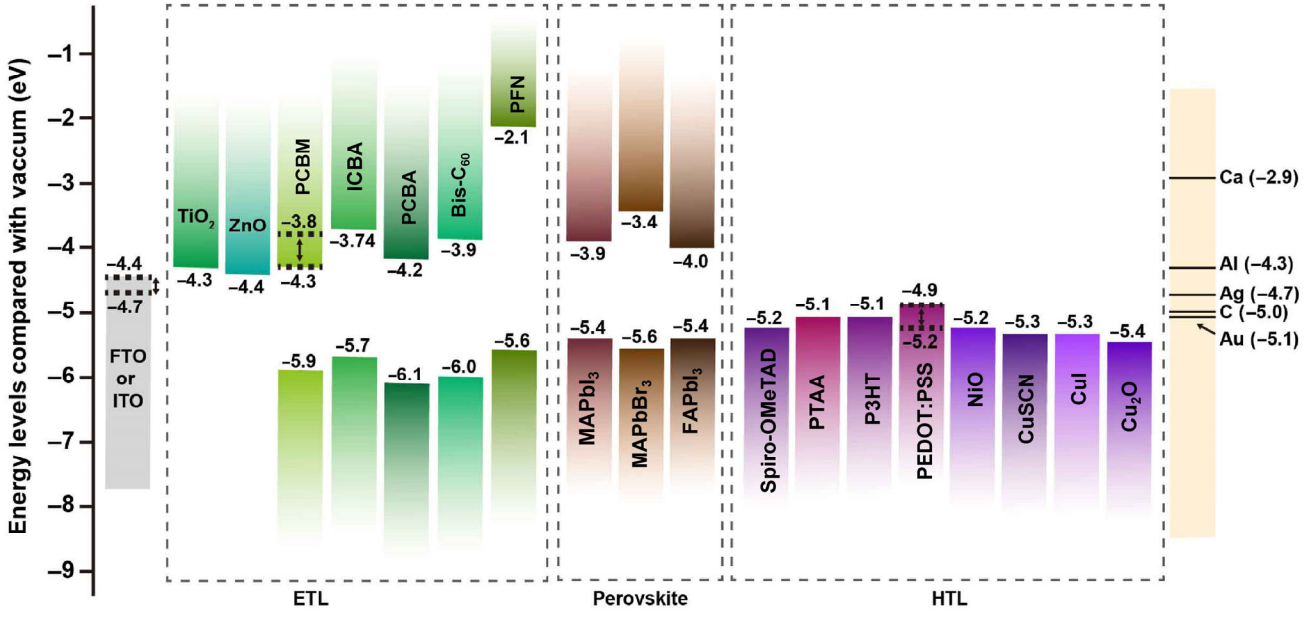

Figure 2 Schematic of literature values of the energy-level alignment for commonly used materials in lead-halide PSCs, including the FTO/ITO substrate, ETLs, perovskite absorbers, HTLs, and counter electrodes.

3 Interface engineering by modification of perovskite, ETL, and HTL

3.1 Modification of perovskite absorber

Imperfections in lead-halide perovskite films, such as grain boundaries, defects, and traps, detrimentally cause recombination loss and the reduction of the PCE in solar cells [28]. The grain boundaries in lead-halide perovskite polycrystalline films have been shown to be far more benign than in those other types of polycrystalline solar cells based on silicon, CdTe, CIGS, etc. Huang et al. showed that ion migration in polycrystalline perovskites dominated through grain boundaries [29]. The penetration of water molecules into perovskite films arises from the diffusion of water molecules along the grain boundaries [30]. Considerable efforts have been made to improve the film quality and enhance the optoelectronic properties of lead-halide perovskite absorbers, such as including additives (polymers, acetate salts, fullerene derivatives, alkylphosphonic acid ω-ammonium chlorides, etc.) in the precursor [31–39], compositional engineering (applying mixed cations [40–45] and mixed halides [46–52]), solvent engineering [53–61], and film-fabrication methodology optimization (one-step and two-step solution processing, vacuum deposition, vapor-assisted solution processing, etc.) [62–71]. Many of these methods aim to trigger homogeneous nucleation at the surface of the previously formed layer to obtain a smooth perovskite film with high surface coverage [37].

In the case of including additives in the perovskite precursor, Liang et al. demonstrated that the crystallization rate of $CH_3NH_3PbI_{3-x}Cl_x$ can be controlled by incorporating a 1,8-diiodooctane (DIO) additive into the precursor solution [32]. The DIO chelation of Pb^{2+} encourages homogenous nucleation and modifies the PEDOT:PSS/$CH_3NH_3PbI_{3-x}Cl_x$ interfacial energy, making it more favorable for perovskite crystals to grow in contact with PEDOT:PSS. As shown in Fig. 3(a), a device processed from a precursor containing 1 wt.% DIO exhibited a ~30% PCE enhancement. Wang et al. blended a $CH_3NH_3PbI_3$ perovskite with the fullerene derivative $A_{10}C_{60}$, where A is a carboxylic-acid group regiospecifically functionalized on the C_{60} head, which imparts hydrophilicity to C_{60} [33]. The energy levels

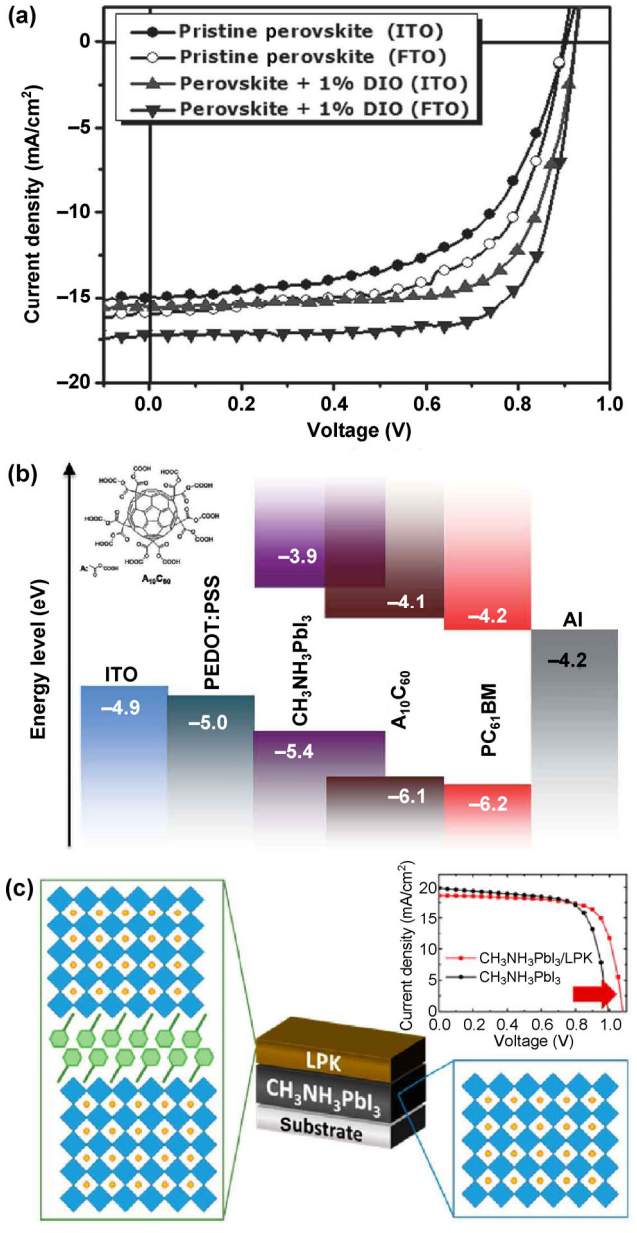

Figure 3 Several modifications of the perovskite absorber. (a) Current–voltage (*I*–*V*) characteristics of a $CH_3NH_3PbI_{3-x}Cl_x$ perovskite with/without 1 wt.% DIO additives in the perovskite precursor. Reproduced with permission from Ref. [32], © WILEY-VCH 2014. (b) Energy levels of bulk heterojunction PSCs. Reproduced with permission from Ref. [33], © The Royal Society of Chemistry 2015. (c) Schematic of the crystal structures of $CH_3NH_3PbI_3$ and a layered perovskite (LPK) and the optimized solar-cell performance. Reproduced with permission from Ref. [43], © American Chemical Society 2016.

of the obtained bulk heterojunction solar cell are shown in Fig. 2(b). The bulk heterojunction interpenetrating network facilitates efficient electron extraction from the composite due to the enlarged interface areas

between $CH_3NH_3PbI_3$ and $A_{10}C_{60}$, which is also a perfect cure for the unbalanced electron–hole diffusion length [10].

The unit cell of lead-halide perovskites (ABX_3) has five atoms in a cubic structure (α phase). The $CH_3NH_3PbI_3$ perovskite undergoes a reversible cubic (α phase)-to-tetragonal (β phase) transition at ~56 °C [72]. This transition is partially responsible for the instability of the $CH_3NH_3PbI_3$ perovskite. To maintain a high-symmetry cubic structure, cation A must fit into the space formed by four adjacent corner-sharing BX_6 octahedra. The tolerance factor $t = (R_A+R_B)/[\sqrt{2}(R_X+R_B)]$ and the octahedral factor $\mu = R_B/R_X$ should retain $0.813 \leqslant t \leqslant 1.107$ and $0.422 \leqslant \mu \leqslant 0.895$, where R_A, R_B, and R_X are the effective ionic radii of A, B, and X, respectively [73]. Otherwise, the cubic structure is distorted. When the A cation is occupied by long-chain alkyl amine anions that are too large, the perovskite becomes a two-dimensional (2D) layered structure [41]. Regarding the compositional engineering of lead-halide perovskites, the most-studied cations for the A site are $CH_3NH_3^+$ (methylammonium or MA, ionic radius: 1.8 Å) and $HC(NH_2)_2^+$ (formamidinium or FA, ionic radius: 1.9–2.2 Å) [45]. Pellet et al. demonstrated for the first time the gradual substitution of MA with FA cations—$(MA)_x(FA)_{1-x}PbI_3$ (where x = 0–1) [40]. Recently, $(FAPbI_3)_{0.85}(MAPbBr_3)_{0.15}$ was reported to have advantages over other systems such as $FAPbI_3$ and $MAPb(I_{0.85}Br_{0.15})_3$ [42]. Notably, the self-assembly of an LPK on an intact $CH_3NH_3PbI_3$ layer induces reorganization of the perovskite interface (Fig. 3(c)), leading to a reduced charge recombination at the interface of $CH_3NH_3PbI_3$ and spiro-OMeTAD [43]. To convert the top layer of $CH_3NH_3PbI_3$ into a layered structure, isopropanol containing phenylethylammonium iodide or n-butylammonium is used. The enormous variety of organic cations offers a promising venue for fine-tuning and controlling the interfaces.

Generally, N,N-dimethylformamide, dimethyl sulfoxide (DMSO), γ-butyrolactone (GBL), and N-methyl-2-pyrrolidone (NMP) are used as effective solvents for both lead halides and CH_3NH_3I. With simple spin-coating, it is almost impossible to obtain a homogeneous and uniform perovskite layer. However, 100% surface coverage is the prerequisite for an optimized interface to suppress recombination loss. To clarify the influence of solvent engineering, Jeon et al. used a mixed solvent of GBL and DMSO and applied toluene drop-casting, forming an extremely uniform and dense perovskite absorber layer via a CH_3NH_3I-PbI_2-DMSO intermediate phase [59]. Recently, Cao et al. disentangled the molecular structures of intermediates for the fabrication of high-quality perovskite films with DMSO as the solvent [56].

The remnant PbI_2 in the film-fabrication process and PbI_2 deliberately introduced can fill the perovskite grain boundaries and act as a blocking layer between TiO_2 and the perovskite interface, reducing the number of trapping sites and the probability of back electron transfer [74–76]. These findings show that the use of a stoichiometric ratio of MAI:PbI_2 precursors is unnecessary.

3.2 Modification of ETL

TiO_2 has been most frequently used as an inorganic electron-transport material in PSCs, owing to its favorable energy level, low cost, and robust fabrication. The electron injection from a perovskite absorber to a TiO_2 ETL is very fast; however, the electron recombination is severe because of the low electron mobility and poor transport properties [80]. In addition, the relatively high density of trap states of TiO_2 reduces the solar-cell efficiency and stability. Most PSCs with TiO_2 require high-temperature sintering, which hinders the applications of these devices.

To engineer the interface between TiO_2 and the perovskite absorber, different TiO_2 nanostructures, such as nanorods, nanowires (NWs), nanotubes, and hierarchical nanostructures have been reported to be effective for extracting electrons and filling the perovskite absorber [77, 81, 82]. As shown in Fig. 4(a), Wu et al. reported TiO_2 with different dimensionalities: zero-dimensional nanoparticles, one-dimensional NWs, and 2D nanosheets. By employing a bi-layered TiO_2 blocking layer, the subsequent hierarchical TiO_2 structure yielded PSC devices with a PCE exceeding 16% [77].

The optical/electrical characteristics of TiO_2 can be easily tuned by doping. Appropriate substitutions of Ti with Y^{3+}, Mg^{2+}, Zn^{2+}, Sn^{4+}, Nb^{5+}, Al^{3+}, Nd^{3+}, and Zr^{4+} have been demonstrated [78, 79, 83]. Doping TiO_2 with Y^{3+} (Fig. 4(b)) favored the efficient extraction of photogenerated charge carriers without inducing excessive

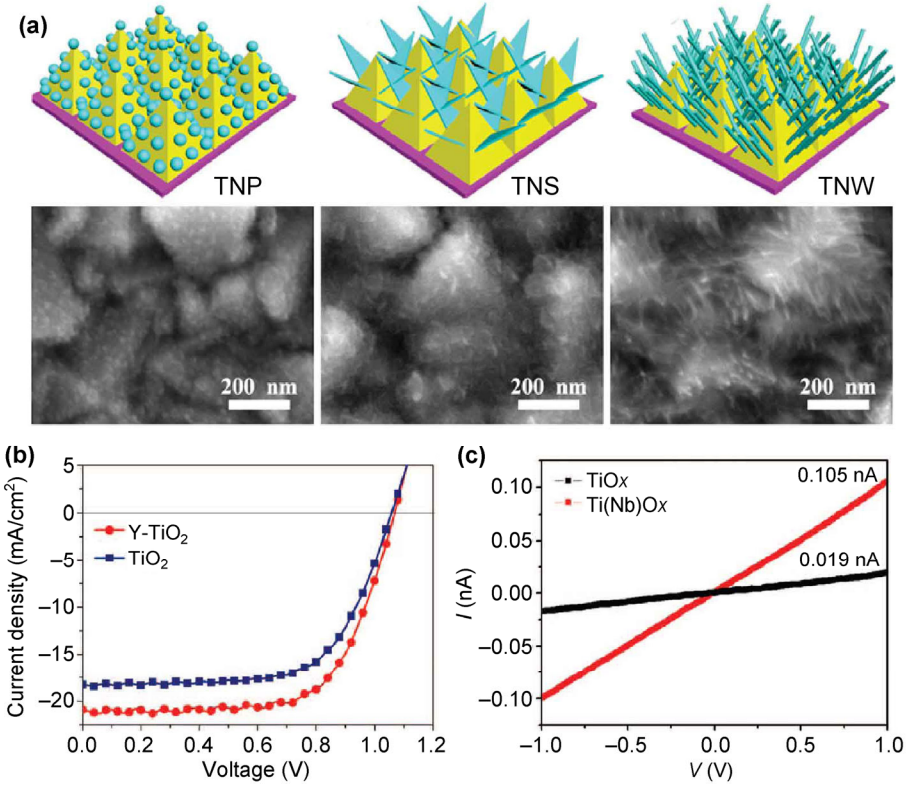

Figure 4 Several modifications of TiO_2 ETL. (a) Schematics and scanning electron microscopy images showing a TiO_2 ETL with dimensionalities, TiO_2 nanoparticles (TNPs), TiO_2 nanosheets (TNSs), and TiO_2 nanowires (TNWs). Reproduced with permission from Ref. [77], © WILEY-VCH 2016. (b) Current density–voltage (*J*–*V*) curves of devices with Y-doped TiO_2 and undoped TiO_2. Reproduced with permission from Ref. [78], © Science (AAAS) 2014. (c) *I*–*V* curves obtained by scanning probe microscopy measurements of a $Ti_{0.95}Nb_{0.05}O_x$ film deposited on PCBM-ITO glass. Reproduced with permission from Ref. [79], © Science (AAAS) 2015.

interface recombination or inhibiting quasi-Fermi level splitting in a perovskite absorber [78]. Modification of ITO by an ultrathin polyethyleneimine ethoxylated (PEIE) layer, inducing a surface dipole, reduced the work function of the ITO from 4.6 to 4.0 eV. This shift was beneficial for electron transport from the TiO_2 ETL to the ITO. The ultimate efficiency of the obtained device was 19.3%, and its average PCE was 16.6%. Wang et al. systematically investigated the effect of adding a series of acetylacetonate-based additives to interact with TiO_2, among which Zr^{4+} was found to be the most effective, yielding an average-efficiency increase from 15.0% to 15.8% [83]. Nb^{5+} doping of TiO_2 can reduce the interfacial electron transfer resistance between PCBM and Ag, increasing the photocurrent, especially in the 0.7–1.0 V forward-bias region (Fig. 4(c)). A fabricated $Ti_{0.95}Nb_{0.05}O_x$ ETL effectively shielded a perovskite absorber from the intrusion of humidity [79].

Despite the perceived advantages of TiO_2, investigations of alternative inorganic ETLs such as ZnO [84], SnO_2 [85, 86], WO_3 [87], and CdS [88] persist. ZnO has a better electron mobility (205–300 $cm^2/(V{\cdot}s)$ than TiO_2 yet suffers from chemical instability. ZnO has been chosen as an ETL to isolate perovskite and the Al electrode in all solution-processed inorganic metal oxide ETL/HTL inverted planar PSCs, yielding improved air stability, an average PCE of 14.6 ± 1.5%, and an uncertified maximum PCE of 16.1% [89]. SnO_2 has also emerged as a promising ETL with a wide bandgap and high electron mobility (240 $cm^2/(V{\cdot}s)$) [90] and can be processed at low temperatures [85].

Fullerene and its derivatives, such as $PC_{61}BM$, indene-C_{60} bisadduct (ICBA), and $PC_{71}BM$, are among the most widely used and efficient organic electron-transport materials for PSCs. These materials are ideal for the ETL in inverted planar PSCs because of their low-temperature processing, tunable energy-level alignment, and good electron mobility. Doping PCBM

with an amphiphilic surfactant oleamide prohibits the electron–hole recombination at the perovskite/Ag interface, increasing the cell efficiency from 10.05% to 12.69% [91]. Cetyltrimethylammonium bromide (CTAB)-doped PCBM can induce a favorable interface dipole to lower the work function of a metal electrode, improving the energy-level alignment at the interface between PCBM and the metal electrode [92]. In addition to doping, blending polystyrene (PS) into an PCBM ETL can yield a highly uniform and smooth layer, which better prevents undesirable charge recombination between the perovskite absorber and the top electrode [93].

3.3 Modification of HTL

For conventional structured PSCs, spiro-OMeTAD is the most commonly used HTL. However, pure spiro-OMeTAD suffers from a low conductivity (~10^{-6}–10^{-5} $cm^2/(V·s)$); thus, lithium bis(trifluoromethane sulfonyl) imide (LiTFSI) and 4-tert-butylpyridine (TBP) are typically used as oxidative additives with spiro-OMeTAD. However, the hygroscopic property of LiTFSI worsens the stability of moisture-sensitive perovskite materials, and the TBP corrosion of perovskites has been systematically studied [94]. Li et al. observed that the intercalation of Li^+ from LiTFSI into TiO_2 decreases the V_{oc} of cells [95]. Moreover, a spin-coated spiro-OMeTAD film exhibited a high density of pinholes, forming channels across the perovskite film, which might be the reason why PSCs spin-coated with spiro-OMeTAD often show a rapidly decreasing PCE when exposed to the ambient environment [96]. Considerable attention has been paid to enhancing the stability of spiro-OMeTAD and suppressing the charge recombination at the perovskite/spiro-OMeTAD interface. Vacuum evaporation is suitable for fabricating pinhole-free spiro-OMeTAD films. Jung et al. explored a triple layer of n-doped, intrinsic, and p-doped spiro-OMeTAD (n–i–p) as an HTL, where an n-type dopant (decamethylcobaltocene) and a p-type dopant (tetrafluorotetracyanoquinodimethane) were added [97]. The built-in potential represented by the staircase of HOMOs across the n–i–p spiro-OMeTAD (Fig. 5(a)) minimized the charge-carrier injection barriers and alleviated the hole-extraction losses at the interfaces.

Because spiro-OMeTAD has the detrimental properties of the multiplex synthetic approach—ambient degradation, a high price, and the accumulation of charge carriers—other HTLs featuring methoxyphenylamine functional groups, polyfluorenre derived polymers [100], tetrathiafulvalene derivatives [101], PEDOT:PSS, poly(3-hexylthiophene-2,5-diyl), poly(triarylamine), graphene nanotubes, carbon nanotubes (CNTs), NiO_x, Cu_2O, CuI, and CuSCN have been investigated to rival or even outperform spiro-OMeTAD.

Poly(3-thiophene acetic acid) (P3TAA) has –COOH groups that can interact with perovskites through $–NH_3$ groups, and the diffusion of this component across the P3TAA/perovskite interface, leading to the easy injection of holes from the perovskite to P3TAA chains, has been reported [98]. As shown in the FTIR spectra of the mixture of $CH_3NH_3PbI_3$, $CH_3NH_3PbI_3$, P3TAA, and $CH_3NH_3PbI_3$/P3TAA (Fig. 5(b)), the N–H stretching peak at 3,088 cm^{-1} shifts to 3,126 cm^{-1}, and N–H bending at 1,571 cm^{-1} is nearly eliminated, indicating the interaction between P3TAA and amino groups of $CH_3NH_3PbI_3$. Here, hole transport is facilitated by mixing the perovskite and the HTL by chemical bonding.

PEDOT:PSS and NiO_x are the most widely used HTLs in inverted planar PSCs. PEDOT:PSS is less ideal because of its acidity, hydroscopicity, and insufficient electron-blocking ability [102]. Inorganic compounds have become a burgeoning field of HTL development. NiO_x-based PSCs often show a smaller fill factor (FF) owing to their low conductivity, whereas NiO_x-based PSCs exhibit a higher V_{oc} than PEDOT:PSS. Doping of NiO films with various materials has been reported. Chen et al. developed heavily p-doped $Li_{0.05}Mg_{0.15}Ni_{0.8}O$ to promote the formation of an Ohmic contact at the FTO/$CH_3NH_3PbI_3$ interface by building a staircase energy-level alignment and decreasing the barrier height [79]. Heavily p-doped NiO increased the electron conductivity of NiO and decreased the charge-transport resistance (Figs. 5(c) and 5(d)). Compared with the PEDOT:PSS-based PSC, the V_{oc} was higher by ~100 mV, and the FF of 0.827 was one of the best values reported for PSCs. Hou et al. demonstrated that a low-temperature-processed NiO-based nanocrystal ink (LT-NiO) formed an almost loss-free hole-selective interface for planar heterojunction PSCs [99]. The

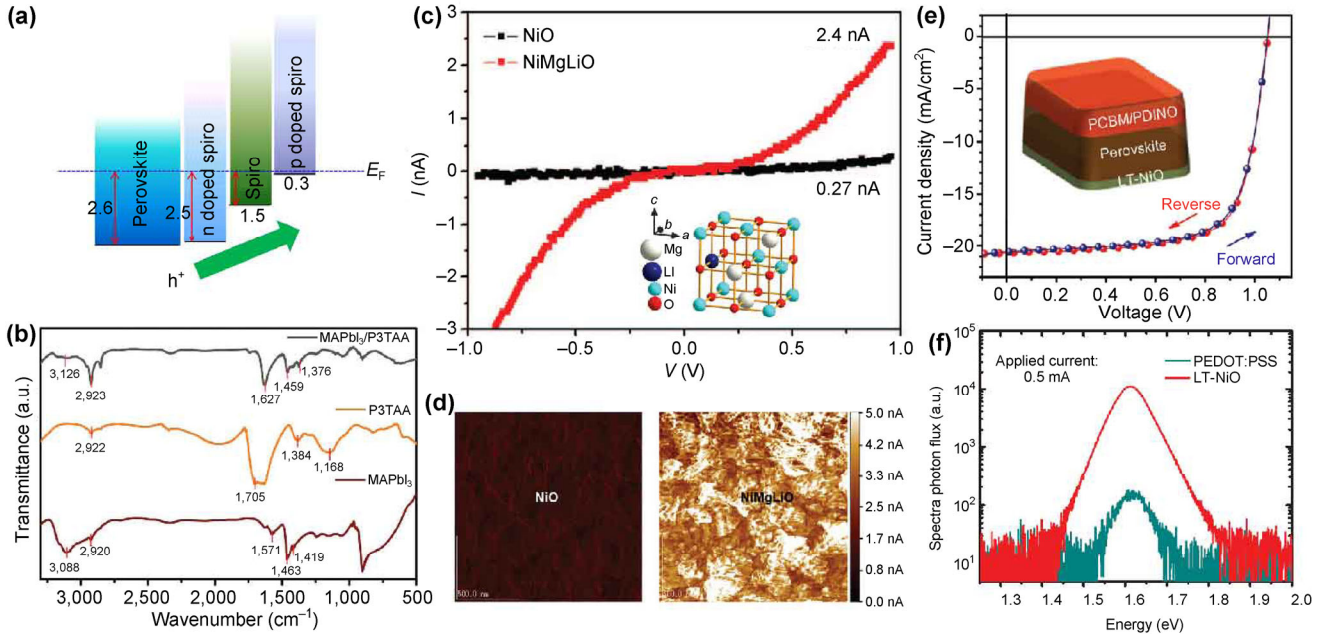

Figure 5 Interface engineering via modification of HTL. (a) Staircase energy-level alignment of n–i–p spiro-OMeTAD extracted from ultraviolet photoelectron spectroscopy (UPS) results. Reproduced with permission from Ref. [97], © Nature Publishing Group 2016. (b) Fourier transform infrared (FTIR) spectra of a mixture of $CH_3NH_3PbI_3$, $CH_3NH_3PbI_3$, P3TAA, and $CH_3NH_3PbI_3$/P3TAA, indicating the interaction between P3TAA and $–NH_3$ in the perovskite. Reproduced with permission from Ref. [98], © The Royal Society of Chemistry 2016. (c) *I*–*V* curves of NiO and $Li_{0.05}Mg_{0.15}Ni_{0.8}O$ films on FTO glass. Inset shows the crystal structure of $Li_xMg_yNi_{1-x-y}O$. (d) Comparison of conductivity-mapping results for NiO and $Li_{0.05}Mg_{0.15}Ni_{0.8}O$ films. Reproduced with permission from Ref. [79], © Science (AAAS) 2015. (e) Inverted planar PSCs with a structure of LT-NiO/perovskite/PCBM/perylene-diimide derivative (PDINO); the device shows minimal hysteresis. (f) EL spectra of PSCs with PEDOT:PSS and LT-NiO HTLs. Reproduced with permission from Ref. [99], © WILEY-VCH 2016.

device efficiency with LT-NiO as the HTL reached 15.2% at forward scan and 15.5% at reverse scan with minimal hysteresis (Fig. 5(e)). The electroluminescence (EL) intensity of the LT-NiO layer was two orders of magnitude higher than that for PEDOT:PSS devices under the same current injection, and the EL spectrum of LT-NiO was broader than that of PEDOT:PSS, indicating suppressed non-radiative losses in PSCs with LT-NiO.

4 Roles of interfacial layers in PSCs

The introduction of interfacial layers into lead-halide PSCs is discussed in this section. The roles of interfacial layers in PSCs can be summarized as follows: (1) the passivation of trap states in the perovskite absorber can alleviate photocurrent hysteresis; (2) subtle energy-level alignment can reduce the energy offset between adjacent layers, thereby increasing the built-in potential and enhancing the charge transport; (3) the protection of the perovskite absorber from moisture can improve the long-term stability of the device and expand its feasibility for PSC applications.

Materials exploited as interfacial layers can be divided into several categories: metal and metal compounds, fullerene and derivatives, graphene and CNTs, self-assembled monolayers (SAMs), small organic molecules, polymers, and quantum dots (QDs).

4.1 Metal and metal compounds

Low-work function metals such as Ca and Ba and alkali metal salts such as LiF can be universally deposited as a buffering layer before the evaporation of the metal electrode, i.e., Au, Ag, or Al. Charge-carrier extraction is improved by reducing the energy barrier via the insertion of such layers in PSCs. By introducing a LiF buffering layer, the FF and J_{sc} of PSCs can be simultaneously improved, and the reverse-scan leakage current can be suppressed [103]. Furthermore, MoO_x is often used as a buffering layer

before the metal electrode. The deposition of MoO_x on $CH_3NH_3PbI_3$ can elevate the valence band (VB) of $CH_3NH_3PbI_3$ towards a higher binding energy to achieve better energy alignment with a spiro-OMeTAD HTL [104].

Wide-bandgap metal oxides (Al_2O_3 [107–110], TiO_2 [111], ZnO [112], MgO [113], Y_2O_3 [114], Cr_2O_3 [115], etc.) are commonly applied as physical blocking layers to substantially decrease the charge losses across interfaces, separate metal corrosion (particularly Ag and Al) caused by halide ions migrating through crystal boundaries in PSC devices, and improve the device stability. To improve the effect of metal oxides, Back et al. integrated an amine-mediated TiO_x (AM-TiO_x) system as an efficient CIL between PCBM and a Ag electrode, which successfully protected the metal electrode by stabilizing the ionic defects migrating from the perovskite absorber (Fig. 6(a)) [105]. The reported solar-cell structure was ITO/PEDOT:PSS/VO_x/$MAPbI_{3-x}Br_x$/PCBM/AM-TiO_x/metal electrode (Ag or Al). The as-prepared inverted planar PSCs maintained almost 90% of their initial PCEs after 4,000 h of storage under N_2 and 80% of their initial PCEs after 200 h of storage in an ambient environment without encapsulation. The amine groups in AM-TiO_x existed in three forms: amine groups without interaction, Ag–amine bonds near the metal interface, and amine–iodide ion bonds near the perovskite absorber, which effectively inhibited the formation of insulation Ag–I bonds across the interface.

Kaltenbrunner et al. improved the device stability by using Cr_2O_3/Cr to shield the top metal electrode from detrimental reactions with oxidizing and iodide species, yielding ultrathin flexible high power-per-weight PSCs for aviation models in ambient conditions [115]. Recently, Guerrero et al. revealed that the S-shape of the *J*–*V* curve is associated with the chemical degradation of the metal contact, which is the major source of perovskite degradation in the absence of moisture (Fig. 6(b)) [6]. They highlighted the importance of cathode protection by Cr_2O_3/Cr. Exposing conventional structured PSCs with Au as the top electrode to 70 ℃ (routinely achieved on a hot day) is enough to induce gold migration through the spiro-OMeTAD

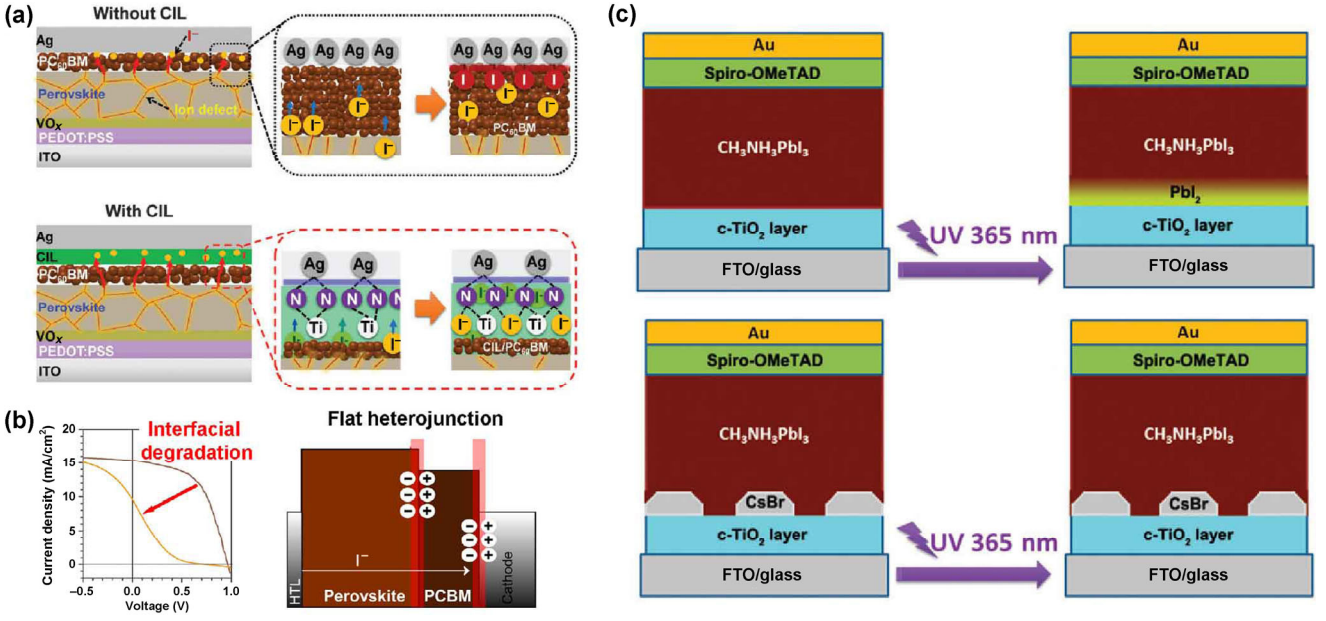

Figure 6 Metal and metal compounds employed for interfacial engineering in lead-halide PSCs. (a) Schematic of fast cathode degradation due to ionic defects and protection by amine-mediated TiO_2 as a chemical inhibition layer (CIL) in a p–i–n planar PSC. Reproduced with permission from Ref. [105], © The Royal Society of Chemistry 2016. (b) Interfacial degradation of inverted planar lead-halide PSCs, where the ionic movement in the perovskite absorber changes the energy profile close to cathode. Reproduced with permission from Ref. [6], © American Chemical Society 2015. (c) Schemes of PSCs with/without a CsBr interfacial layer between compact TiO_2 and the $CH_3N_3PbI_3$ absorber before and after ultraviolet (UV) irradiation. Reproduced with permission from Ref. [106], © The Royal Society of Chemistry 2016.

HTL into the perovskite absorber [116]. By introducing a Cr metal interlayer between the HTL and the Au electrode, long-term losses induced by high temperatures are avoided so that the device can withstand hard thermal stress and be commercially viable.

Cs-based compounds are of vital importance in ETL/perovskite interfacial engineering in PSCs. Cesium carbonate (Cs_2CO_3) was first reported as a new surface-modification material for PSCs (FTO/mesoporous TiO_2 (mp-TiO_2)/$CH_3NH_3PbI_3$ /spiro-OMeTAD/Au) by Dong et al. [117]. The work function of Cs_2CO_3 is 2.2 eV, and a thin insulating Cs_2CO_3 layer between mesoporous TiO_2 and perovskite interface can significantly reduce the charge recombination. In the same year as the study of Dong et al., Hu et al. reported the use of Cs_2CO_3 to modify ITO (referred to as ITO:Cs_2CO_3) for avoiding the use of a compact n-type blocking layer in a planar PSC, yielding a remarkable PCE of 15.1% [118]. The cells were fabricated at a low temperature via a solution-based process. The obtained cells had better stability than TiO_2 ETL-based PSCs because of the avoidance of oxygen vacancies and UV degradation in TiO_2. As shown in Fig. 6(c), a recent report demonstrated the CsBr modification between a compact TiO_2 (c-TiO_2) ETL and the perovskite absorber in a planar heterojunction PSC. The applied CsBr not only decreased the work function of c-TiO_2 from 4.07 to 3.90 eV and improved the average PCE from 11.5% ± 0.6% to 15.3% ± 0.5% but also enhanced the resilience of the perovskite to intense UV exposure [106].

Other metal compounds, such as Sb_2S_3, have also been investigated as an effective surface-blocking layer between TiO_2 and perovskites [119]. Sb_2S_3 can stabilize PSCs against light exposure without any encapsulation, implying that degradation originates at the TiO_2/perovskite interface.

4.2 Fullerene and derivatives

PSCs commonly exhibit anomalous hysteresis in *J*–*V* curves. The origin of the hysteresis is not fully understood, but several possible mechanisms have been proposed, such as ferroelectricity and mobile ionic species [120, 121]. It is perceived that the hysteresis in n–i–p planar PSCs is more severe than that in mesoporous PSCs, and negligible hysteresis has been reported for many p–i–n (inverted) planar PSCs with fullerene derivatives as the ETL.

Shao et al. demonstrated that in inverted planar PSCs, fullerene derivatives on the perovskite absorber can effectively passivate charge traps on the surface and the grain boundaries of the initial annealed perovskite absorber [122]. The spin-coated PCBM layer can intimately cover the perovskite and permeate into the perovskite absorber along the grain boundaries during the thermal-annealing process, which effectively decreases surface charge recombination (Fig. 7(a)). A device with a structure of ITO/PEDOT:PSS/$CH_3NH_3PbI_3$/PCBM/C_{60}/bathocuproine (BCP)/Al exhibited a remarkable PCE enhancement from 7.3% to 14.9%, with a reduced hysteresis, compared with control devices without PCBM. Chiang et al. reported a simple inverted bulk heterojunction perovskite-PCBM solar cell (Fig. 7(b)) with a high FF of 0.82 and a PCE as high as 16.0% with no obvious hysteresis. This device was fabricated via a low-temperature two-step solution process by preparing a PbI_2-PCBM hybrid film and then converting it into bulk heterojunction $CH_3NH_3PbI_3$-PCBM [34]. Adding a small amount of PCBM into the PbI_2 precursor solution was critical for enhancing the quality of the perovskite via the filling of pinholes and vacancies between the perovskite grains. Recently, an inverted planar PSC with a perovskite-PCBM gradient interlayer other than a bulk heterojunction was reported [35]. Molecular PCBM was included in the dripping solvent toluene for the spin-coating of the perovskite precursor solution. The dripping-solvent deposition of molecular PCBM on a perovskite precursor can lead to the formation of a gradient of electron acceptors in the perovskite absorber (Fig. 7(c)), and the hydrophobic characteristic of PCBM reduced the interaction between DMSO solvent vapor and a perovskite intermediate [123]. The conformal PCBM coating on the perovskite absorber in the gradient heterojunction deposition led to a minimized resistive loss in large-area PSCs. A certified PCE of 18.21% for an aperture area of 1.022 cm^2 was obtained.

Fullerene derivatives such as amine-functionalized DMAPA-C_{60} (molecular structure in Fig. 7(d)) [124] and fulleropyrrolidine-based C_{60}-N [125] can also be applied in the interface of the ETL and as a metal electrode in inverted planar PSCs to reduce the work

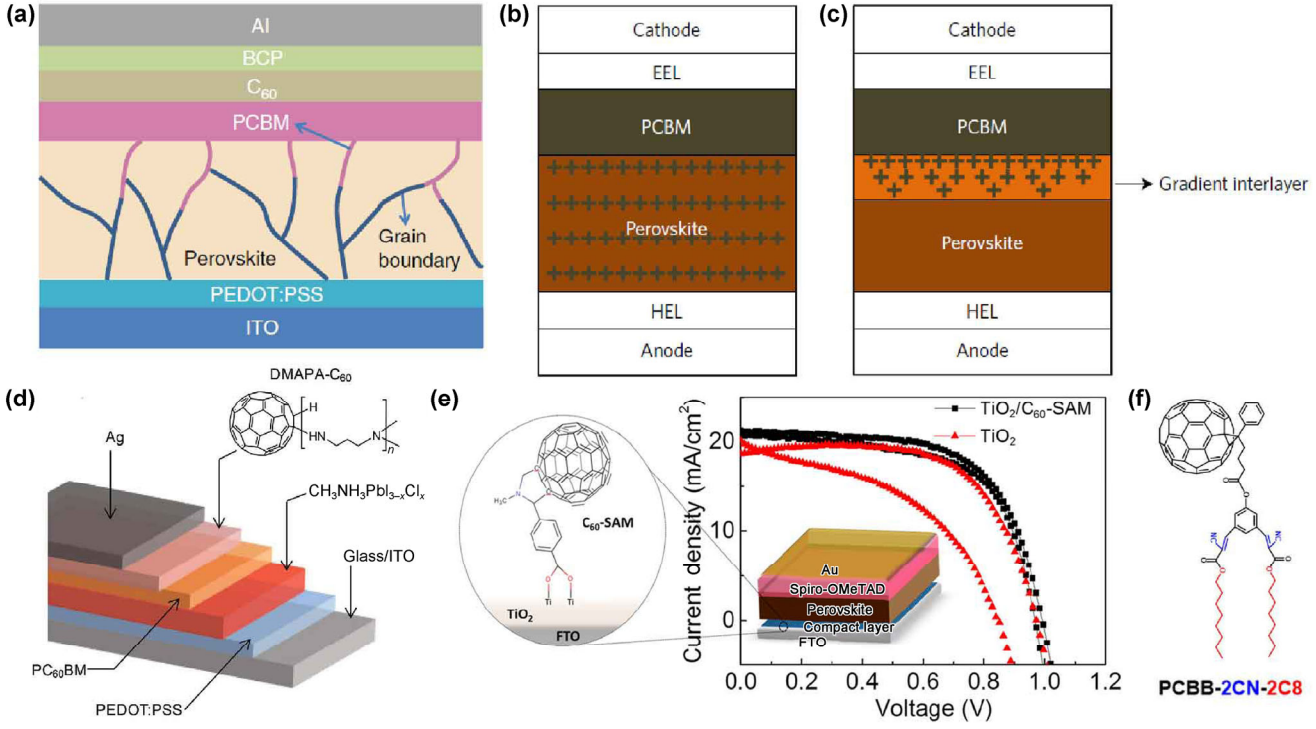

Figure 7 Fullerene and derivatives applied for interfacial engineering in lead-halide PSCs. (a) PCBM permeates along the grain boundaries of the perovskite during thermal annealing. Reproduced with permission from Ref. [122], © Macmillan Publishers Limited 2014. (b) Bulk heterojunction of a perovskite and PCBM. (c) Graded heterojunction of a perovskite and PCBM, where the interlayer is composed of perovskite with a gradient distribution of PCBM. Reproduced with permission from Ref. [34], © Macmillan Publishers Limited 2016. (d) Schematic of the inverted solar-cell with DMAPA-C_{60} interfacial engineering. Reproduced with permission from Ref. [124], © WILEY-VCH 2015. (e) Planar heterojunction PSCs with C_{60}-SAM engineering; the TiO_2/perovskite interface exhibits considerably reduced hysteresis. Reproduced with permission from Ref. [126], © American Chemical Society 2014. (f) Molecular structure of the carefully designed fullerene derivative PCBB-2CN-2C8 for application in the TiO_2/perovskite interface. Reproduced with permission from Ref. [127], © American Chemical Society 2015.

function of the metal electrode and improve the stability of PSCs under ambient conditions.

As in n–i–p planar PSCs, hysteresis is particularly pronounced, which might be due to the depletion region and pinning of the electron quasi-Fermi level across the compact TiO_2/perovskite interface [122]. Fullerene derivatives are used to modify the interface between the TiO_2 ETL and the perovskite absorber to alleviate hysteresis, improve the electron transfer, and enhance the stability of planar PSCs. A fullerene SAM (C_{60}-SAM) (molecular structure in Fig. 7(e)) enhances the electron transfer and passivates the formation of trap states at the TiO_2/perovskite interface by anchoring groups on the TiO_2 surface and via fullerene moiety on the perovskite-absorber surface [126]. A triblock fullerene derivative (PCBB-2CN-2C8) (Fig. 7(f)) with a rational molecular design for modifying the TiO_2/perovskite interface can uplift the work function of TiO_2 and significantly improve the charge extraction, resulting in a 20.7% improvement in the PCE [127]. C_{60} was chosen as the main building block for PCBB-2CN-2C8 because of its high electron affinity. Cyano groups were used for pacifying oxygen vacancies and dioctyloxy chains. The cyano groups were designed to suit the orthogonal solvents used in perovskite-film fabrication. The electrical properties of PCBB-2CN-2C8 suggest that it can reduce the charge-recombination loss due to the deep trap states in TiO_2. [6,6]-phenyl-C_{61}-butyric acid (PCBA) has also been demonstrated as an interfacial layer between compact TiO_2 and a $CH_3NH_3PbI_3$ film to achieve a high V_{oc} of 1.16 V and a maximum PCE of 17.76%, implying that PCBA can serve as a hole-blocking layer to reduce the trap-state density atop compact TiO_2.

4.3 Graphene oxide (GO) and CNTs

GO is a precursor for the synthesis of graphene by chemical or thermal reduction methods. GO exhibits a 2D C–C structure with various oxygen-containing functional groups, such as carboxyl, carbonyl, lactone, phenol, and quinone, mostly at sheet edges. The hydrophilic oxygen-containing groups reduce the electron mobility; thus, GO has potential for suppressing the electron recombination in PSCs. Li et al. reported that the amphiphilic GO functionalization of a perovskite-absorber surface decreased the contact angles from 13.4° to 0° [128]. GO can also interact with the perovskite by Pb–O bonding to suppress unsaturated Pb bonding at the interface, and 2D C–C bonds in GO can absorb spiro-OMeTAD via π–π interactions, which enhances the charge-collection efficiency because of the improved contact between the perovskite and the HTL. The corresponding average PCE of a device with a structure of FTO/c-TiO_2/mp-TiO_2/$CH_3NH_3PbI_3$/GO/spiro-OMeTAD/Au increased from 10.0% (control devices without GO) to 14.5%. Recently, Li-neutralized GO was reported to partially passivate oxygen vacancies of mp-TiO_2 [129] in mesoscopic structured PSCs.

Feng et al. introduced ammonia-modified GO (GO:NH_3) between a PEDOT:PSS HTL and a perovskite in a cell structure of ITO/PEDOT:PSS/GO:NH_3/$CH_3NH_3PbI_{3-x}Cl_x$/PCBM/solution-processed bathophenanthroline (sBphen)/Ag. The PCE of the cell was as high as 16.11% and was far superior to those of control cells without a GO:NH_3 layer [130]. The function of GO:NH_3 was threefold. First, the perovskite exhibited full coverage and substantially improved crystallization; second, the optical absorption of PSC was enhanced; third, improved energy alignment between PEDOT:PSS and perovskite layer was enabled by GO:NH_3. Moreover, the stability of these PSCs was greatly enhanced in an ambient environment.

In several studies, multiwalled carbon nanotubes and single-walled carbon nanotube (SWCNTs) have been employed to extract holes in PSCs [131–133]. Ihly et al. demonstrated that with only 5 nm of a highly enriched SWCNT film at the interface between a perovskite and spiro-OMeTAD enabled sub-picosecond hole extraction from the perovskite and slow back transfer (hundreds of microseconds) [134]. This result indicates that the pairing of organic and inorganic HTLs via interfacial SWCNTs is an economical method for the fabrication of PSCs.

4.4 SAMs

The literature reveals that SAMs can modify the interface between commonly used ETLs and perovskites. Substrates covered with amino or ammonium groups can promote the growth of smooth and highly crystalline perovskite films. This phenomenon is probably due to the enhanced affinity induced by hydrogen bonding or electrostatic interactions between these functional groups and the perovskite framework [135]. In 2014, Ogomi et al. designed amino-acid HI-salt ($HOCO–R–NH^{3+}I^-$) monolayers as an anchor for mesoscopic PSCs. Glycine, β-alanine, and γ-amino butyric acid HI salts were employed as the anchoring group, and the results indicated that $HOCO–R–NH^{3+}I^-$ with longer alkyl chains were better absorbed on the TiO_2 surface because of the better self-organization of alkyl groups [136]. The effects of the $HOCO–R–NH^{3+}I^-$ monolayer include the passivation of surface traps on porous TiO_2, corresponding to the better growth of the perovskite absorber, better energy alignment due to the surface dipole, and the retardation of charge recombination by alkyl groups. Similarly, a 3-aminopropanioc acid SAM (C3-SAM)-functionalized ZnO ETL (Fig. 8(a)) was reported to improve the crystallinity of a perovskite film and reduce the pinholes and charge traps. The PCE was enhanced by 31% (up to 15.67%) [134]. TiO_2 functionalized with glycine [137] and an amino-propyltrimethoxysilane SAM [135] has also been reported (Fig. 8(b)). The self-assembly of the amino-silane monolayer can be realized by the formation of covalent bonds through condensation reactions between alkoxy groups in silane and hydroxyl groups at the surface of TiO_2. In addition to amino and ammonium groups, thiols can be applied in the SAM at the TiO_2/perovskite interface to enhance the performance and stability of PSCs. In particular, HOOC-Ph-SH facilitated the growth of larger perovskite crystallites and enhanced the transfer of electrons across the TiO_2/perovskite interface, and

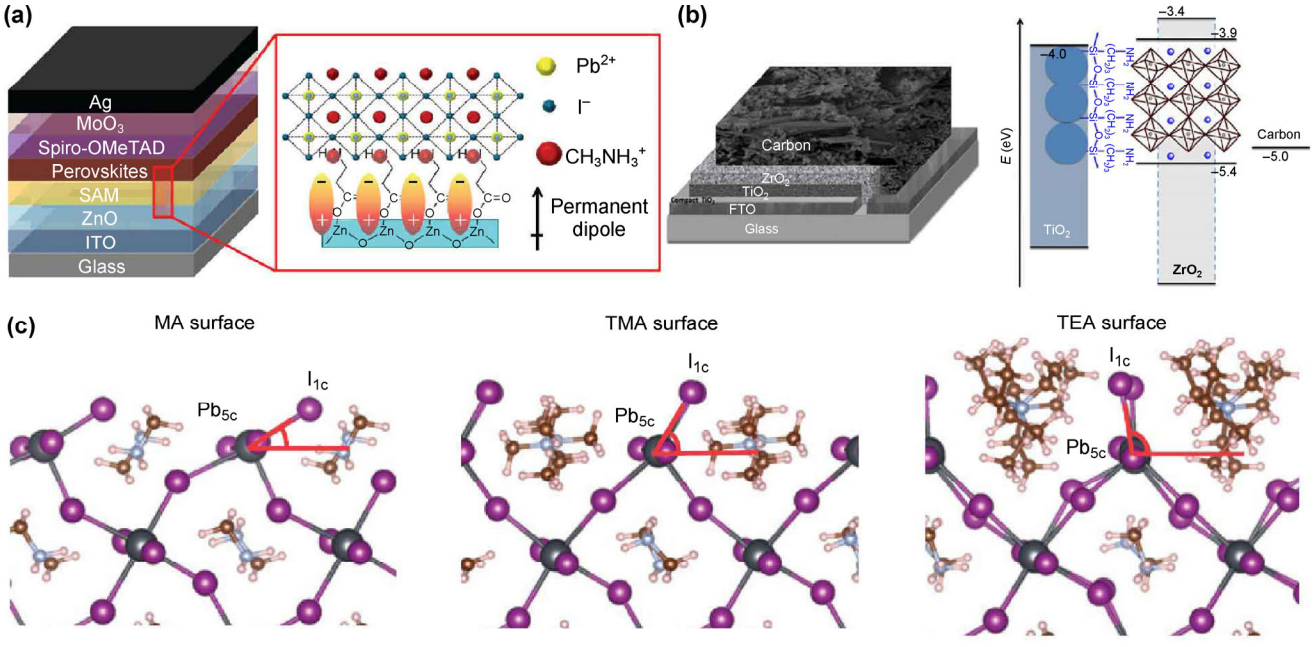

Figure 8 SAMs applied for interface engineering in lead-halide PSCs. (a) Schematic of a C3-SAM-functionalized PSC, C_3-SAM-induced permanent dipole formation, and the improved crystallinity of perovskite crystals. Reproduced with permission from Ref. [134], © American Chemical Society 2015. (b) Structure of a fully printable mesoscopic PSC with a carbon counter electrode. The energy-level diagram and the interfacial amino-organic silane between TiO_2 and perovskite are also shown. Reproduced with permission from Ref. [135], © American Chemical Society 2015. (c) Side views of optimized geometries of the (100) surfaces of pristine perovskite (MA)-, tetra-methyl ammonium (TMA)-, and tetra-ethyl ammonium (TEA)-functionalized perovskites. Reproduced with permission from Ref. [139], © Macmillan Publishers Limited 2016.

the hydrophobic thiol HS-PhF_5 remarkably improved the stability of PSCs, which retained over 80% of their initial efficiency after 10 days of storage at a humidity of ~45% [138].

SAMs have also been applied on the surface of perovskite absorbers to make the cell more immune to moisture, e.g., C_{12}-silane with an insulating alkyl chain [140]. Recently, Yang et al. demonstrated an inspiring functionalization of perovskite thin films via moisture-tolerant molecules [139]. Hydrophobic alkyl ammonium cations were assembled on the perovskite surface as a water-resisting layer, and the functionalized perovskite exhibited a superior moisture stability (90% ± 5%) over 30 days. The ammonium cations investigated were categorized into three groups: type I cations with only one methyl group, type II cations with three or four methyl groups, and type III cations with four alkyl groups. As shown in Fig. 8(c), the steric effect induced by bulky hydrophobic ammonium cations caused the tilt angles of the perovskite surface Pb_{5c}–I_{1c} (Pb_{5c} represents the surface five-coordinated Pb atoms, and I_{1c} represents surface I atoms coordinated with only one Pb atom) bonds to increase from 34.7° to 98.7°, hindering the reaction of water molecules with Pb_{5c} atoms, which enhanced the stability of the perovskite layer. This work introduced a new avenue for commercial devices that operate in ambient conditions.

4.5 Small organic molecules and polymers

It has been well perceived that efficient PSCs can be fabricated with an inverted planar heterojunction, in which perovskite is usually sandwiched between a PEDOT:PSS or NiO_x HTL and a PCBM ETL. However, this inverted p–i–n structure has not yet achieved a comparable PCE to conventional structures with high-temperature sintered metal-oxide ETLs. One reason for this is the energy offset between the Fermi level of high-work function metals (Ag, Au, Al) and the LUMO of the organic ETL (PCBM). In this regard, the thermal evaporation of LiF [103], Ca [141], BCP [142], and C_{60} [143] on the PCBM layer is commonly

applied, substantially improving the FF. However, high-vacuum processing is required for the thermal evaporation of these layers. Pablo et al. first reported a low-temperature solution processed n-type TiO_x layer between PCBM and Al, which highlighted the focus of developing solution-processed cathode interlayers for inverted planar PSCs. Since then, organic molecules such as PDINO [144], sBphen [145], rhodamine 101 zwitterion [146], 4,7-diphenyl-1,10-phenanthroline doped with bis(2-methyldibenzo-[f,h]quinoxaline) (Bphen:$Ir(MDQ)_2(acac)$) [147] and solution-processed BCP [148], titanium (diisopropoxide) bis(2,4-pentanedionate [149], as well as polymers such as PEIE [150], poly[3-(6-trimethylammoniumhexyl) thiophene] [150], the amino-functionalized polymer PN4N [151], the polyfluorene derivative PFN [151], and poly(2-ethyl-2-oxazoline) [152], have been reported as buffering layers between PCBM and the metal electrode. These materials (molecular structures shown in Fig. 9) can all be applied on PCBM via low-temperature solution processing and lead to a reduced leakage current and high FF.

In addition to being used as buffering layer between PCBM and metal electrode, polymers such as 4-lithium styrenesulfonic acid/styrene copolymer (LiSPS) [153], PS, Telfon, and polyvinylidene-trifluoroethylene [154] have been employed to engineer the interface between the perovskite and the fullerene ETL. LiSPS ionomers can fill the pinholes of solution-processed perovskite, leading to an optimized contact between the perovskite and a PCBM ETL, as indicated by a reduced leakage current. Huang et al. investigated several polymers as a thin insulating tunneling interlayer between a perovskite and C_{60} for efficient and water-resistant PSCs [154]. The polymer tunneling layer suppressed the charge recombination and protected the perovskite from moisture. Furthermore, this polymer insulating layer did not require lattice matching, enabling freedom in the device design.

4.6 QDs

Although QDs have been widely applied in various types of solar cells owing to their tunable bandgaps and high absorption coefficients, their applications in lead-halide PSCs have been limited. Yang et al. examined the effects of graphene QDs inserted as an ultrathin interlayer between a TiO_2 ETL and a perovskite. The obtained PSCs underwent an efficiency enhancement caused by fast electron extraction due to graphene QDs [155]. Figure 10(a) shows the device structure, energy-level alignment, and graphene-QD structure determined by theoretical calculations. The PCE of the mesoscopic PSC increased from 8.81% (without graphene QDs) to 10.15% (with graphene QDs) (Fig. 10(b)). The effect of the graphene QDs was mostly reflected by an increased J_{sc}. Ultrafast transient absorption spectroscopy measurements indicated shorter electron-extraction times of 90–106 ps across

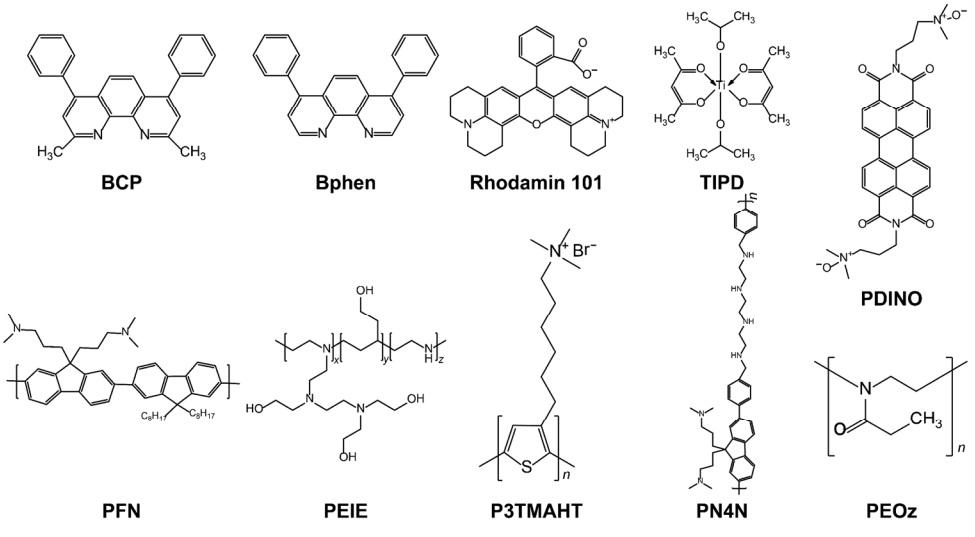

Figure 9 Molecular structures of several organic molecules and polymers that can be applied as an interlayer between PCBM and the metal electrode via solution processing.

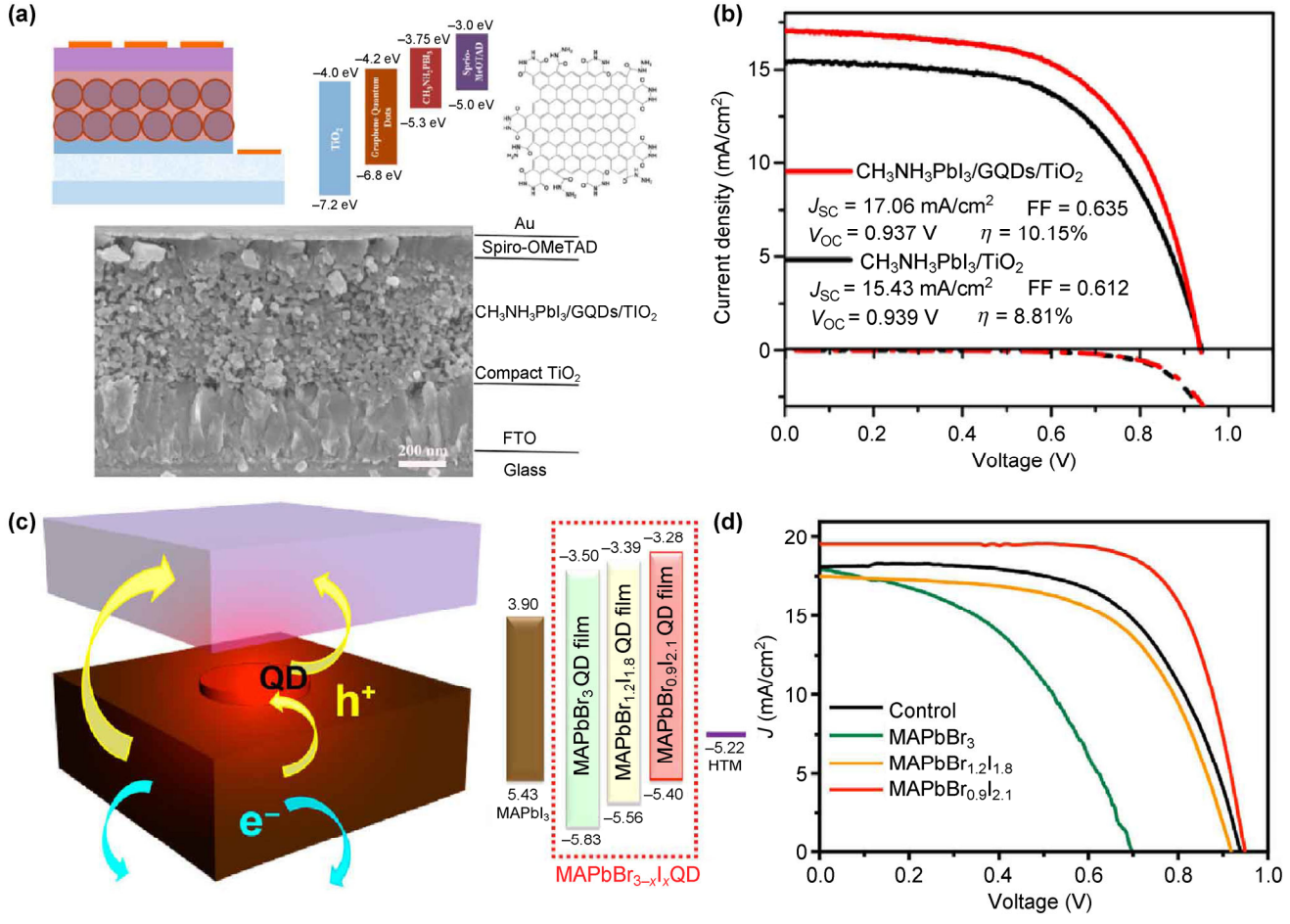

Figure 10 QDs applied for interface engineering in lead-halide PSCs. (a) and (b) Schematic of mesoscopic PSCs with a graphene QD interlayer between the TiO_2 and perovskite. The theoretical calculated structure of the graphene QDs is also presented. Reproduced with permission from Ref. [155], © American Chemical Society 2014. (c) and (d) Schematic of the structure and the energy-level alignment of planar PSCs incorporating $CH_3NH_3PbBr_{3-x}I_x$ QDs between the perovskite and spiro-OMeTAD. Reproduced with permission from Ref. [157], © American Chemical Society 2016.

the perovskite/graphene QDs/TiO_2 and 260–307 ps across perovskite/TiO_2, suggesting accelerated electron injection induced by the graphene QDs. Reduced graphene QD-modified ZnO has also yielded faster electron transfer [156].

Recently, PbS QDs were reported to be incorporated into planar PSCs as an efficient inorganic HTL, with the merits of extending the whole absorption spectrum of the cells into the infrared region [158, 159]. However, the engineering of perovskite/HTL interface using QDs is highly intriguing. Cha et al. reported the interface engineering of planar heterojunction PSCs by introducing $CH_3NH_3PbBr_{3-x}I_x$ QDs between the perovskite and the spiro-OMeTAD HTL without introducing any other foreign components [157]. The synthesis of organometallic halide perovskite QDs was reported by Feng et al. [160]. By adjusting the Br:I ratio in the synthesized $CH_3NH_3PbBr_{3-x}I_x$ QDs, tunable fluorescence and VB edges were obtained. When the VB edge of the $CH_3NH_3PbBr_{3-x}I_x$ QDs was between that of the perovskite and spiro-OMeTAD, hole transfer from the perovskite film into the HTL was facilitated. Otherwise, when the VB of the $CH_3NH_3PbBr_{3-x}I_x$ QDs was below that of perovskite, hole transfer was hindered by the inappropriate energy-level alignment (Figs. 10(c) and 10(d)). Mixing $CH_3NH_3PbBr_{3-x}I_x$ QDs in the perovskite framework during the anti-solvent one-step coating process led to inferior PCEs, probably owing to the large number of recombination spots caused by the difference

of VB levels between bulk perovskite and the $CH_3NH_3PbBr_{3-x}I_x$ QDs. This work may introduce new avenues for interface engineering in PSCs and the application of organometallic halide perovskite QDs.

5 Summary and outlook

We comprehensively summarized the recent progress in interfacial engineering for lead-halide PSCs from the perspective of the material modification of each single layer (perovskite absorber, ETL, and HTL), along with the roles of categorized materials that can be introduced into PSCs as interlayers (Table 1). The main expected functions of tailoring the interfaces in PSCs are summarized as follows: proper energy-level tailoring between adjacent layers to reduce the energy offset; enhancement of the electrical conductivity and wettability of the ETL and HTL; the passivation of trap states in the ETL and perovskite films; and the protection of the perovskite from moisture.

The excellent properties of the lead-halide perovskite make it a promising material for solar-to-electricity conversion. Owing to the passion of researchers in film fabrication worldwide, mechanism investigations, composition explorations, and interface engineering, the PCE of PSCs can now compete with those of CIGS, CdTe, and Si solar cells. However, the stability of PSCs under real-application operating conditions, such as a relatively high temperature and maximum power output, are still far from sufficient and from satisfying the requirements of standard stability tests JISC8938, 1995 and IEC61646, 2008. Further imminent breakthroughs must focus on the stability of PSCs. The successful protection and integration of perovskite-based photoanodes and cathodes in electrolyte have been reported. For instance, encapsulation by Ni [178] and InBiSn alloy [179] (Fig. 11) has been proven effective, even in water. Ni can serve as both a physical passivation barrier and a hole-transferring catalyst, and the InBiSn alloy can effectively shield the perovskite

Table 1 Performance of lead-halide PSCs with interfacial layers

Device structure	J_{sc} (mA/cm^2)	V_{oc} (mV)	FF	PCE (%)	Remarks	Ref.
ITO/PEDOT:PSS/BHJ $CH_3NH_3PbI_3$–PCBM/PCBM/Ca/Al	20.2	970	0.82	16.0	Buffering layer	[34]
ITO/PEDOT:PSS/ $CH_3NH_3PbI_3$/PCBM/LiF/Al	20.7	866	0.78	14.1	Buffering layer	[103]
FTO/PEDOT:PSS/$CH_3NH_3PbI_{3-x}Cl_x$/PCBM/TiO_x/Al	15.8	940	0.66	9.8	Achieving a stable electronic contact with top Al electrode	[111]
ITO/PEDOT:PSS/ $CH_3NH_3PbI_{3-x}Cl_x$/PCBM/ZnO/Al	20.5	970	0.80	15.9	Improving hole-blocking capability, preventing direct contact of Al and perovskite layer and enhance ambient stability of devices	[112]
FTO/NiLiMgO/$FA_{0.85}MA_{0.15}Pb(I_{0.85}Br_{0.15})_3$/gradient interlayer/PCBM/Ti(Nb)O_x/Ag	21.95	1,081	0.78	18.21	Improving electron collection and reducing recombination loss	[35]
ITO/PEDOT:PSS/VO_x/$CH_3NH_3PbI_{3-x}Br_x$/PCBM/AM-TiO_x/Ag	18.34	1,070	0.82	16.09	Stabilizing ionic defects migrating from the perovskite layer	[105]
ITO,PET/PEDOT:PSS/$CH_3NH_3PbI_{3-x}Cl_x$/PTCDI,PCBM/Cr-Cr_2O_3/Au,Al/PU	17.5 ± 1	930 ± 40	~0.80	12.5 ± 1	Protecting metal top contacts from reactions with perovskite	[115]
FTO/TiO_2/$CH_3NH_3PbI_3$/Al_2O_3/Au	10.67	789.2	0.60	5.07	Promoting carrier transportation, suppressing recombination of free carriers	[107]
FTO/TiO_2/$CH_3NH_3PbI_3$/Al_2O_3/spiro-OMeTAD/Au	11.11	860	0.46	4.60	Protecting $CH_3NH_3PbI_3$ from moisture and retarding charge recombination	[108]
FTO/c-TiO_2/(mp-TiO_2+$CH_3NH_3PbI_3$)/AlO_x/Au	17.62	921	0.68	11.10	Electron blocking layer	[161]
FTO/c-TiO_2/mp-TiO_2/Al_2O_3/$CH_3NH_3PbI_{3-x}Cl_x$/spiro-OMeTAD/Au	20.1	960	0.66	12.7	Suppressing back electron transfer	[110]
FTO/c-TiO_2/mp-TiO_2/$CH_3NH_3PbI_3$/MoO_x/spiro-OMeTAD/Ag	22.06 ± 0.4	900 ± 120	0.59 ± 0.09	11.2 ± 0.8	Inducing highly crystalline perovskite film and MoO_x interfacial layer simultaneously	[104]
ITO/Cs_2CO_3/$CH_3NH_3PbI_3$/spiro-OMeTAD/Au	19.9	1,070	0.71	15.1	Achieving efficient electron-selective contact between perovskite and ITO without compact n-type metal oxide blocking layers	[118]
FTO/ZnO/AZO/$CH_3NH_3PbI_3$/spiro-OMeTAD/Au	19.77	900	0.60	10.7	Suppressing charge recombination at ZnO/$CH_3NH_3PbI_3$ interface	[162]
FTO/ TiO_2/Y_2O_x/$CH_3NH_3PbI_2Cl$/spiro-OMeTAD/Ag/Au	16.55	790	0.71	7.53	Retarding charge recombination	[114]

(Continued)

Device structure	J_{sc} (mA/cm^2)	V_{oc} (mV)	FF	PCE (%)	Remarks	Ref.
ITO/PEDOT:PSS-GeO_2-CH_3NH_3I:$PbCl_2$/PCBM/Ag	21.55	960	0.74	15.15	Improving ambient stability, growing sites of crystal nucleus of perovskite films, facilitating carrier transport pathway	[163]
FTO/c-TiO_2/(MgO@TiO_2+$CH_3NH_3PbI_3$)/spiro-OMeTAD/Ag	20.02	890	0.71	12.7	Retarding charge recombination	[164]
FTO/TiO_2/MgO/$CH_3NH_3PbI_3$/spiro-OMeTAD/Au	19.16	1,056	0.69	13.94	Retarding back recombination and improving stability	[113]
FTO/mp-TiO_2/Cs_2CO_3/$CH_3NH_3PbI_3$/spiro-OMeTAD/Au	21.3	1,030	0.65	14.2	Improving electron transport and retarding back recombination	[117]
FTO/c-TiO_2/CsBr/$CH_3NH_3PbI_{3-x}Cl_x$/spiro-OMeTAD/Au	19.8 ± 0.7	1,040 ± 20	0.74 ± 0.03	15.3 ± 0.5	Enhancing UV-stability, alleviating defects at perovskite-titania heterojunction, enhancing electron extraction	[106]
FTO/c-TiO_2/mp-TiO_2/$CH_3NH_3PbI_3$/$Li_4Ti_5O_{12}$/spiro-OMeTAD/Au	20.7	1,000	0.73	15.1	Insulating layer, reducing carrier recombination	[95]
FTO/TiO_2/Sb_2S_3/$CH_3NH_3PbI_3$/CuSCN/Au	17.04	560	0.53	5.03	Protecting $CH_3NH_3PbI_3$ from degradation under light exposure	[119]
FTO/TiO_2/C_{60}-SAM/$CH_3NH_3PbI_{3-x}Cl_x$/spiro-OMeTAD/Au	22.1	1,040	0.75	17.3	Enhancing electron transfer, passivating formation of trap states and reducing nonradiative recombination	[126]
ITO/ZnO/PCBM/$CH_3NH_3PbI_3$/PTB7-Th/MoO_3/Ag	18.18	1,000	0.67	12.2	Suppressing interface charge recombination	[165]
FTO/TiO_x/60-PCBM/$CH_3NH_3PbI_3$/spiro-MeOTAD/Au	20.6	1,100	0.75	17.0	Efficient charge extraction	[166]
ITO/TiO_2/PCBB-2CN-2C8/$CH_3NH_3PbI_xCl_{3-x}$/spiro-OMeTAD/Au	19.85 ± 0.75	1,060 ± 12	0.78 ± 0.01	16.45 ± 0.81	Enhanced charge extraction, surface passivation and improved device stability	[127]
FTO/c-TiO_2/PCBA/$CH_3NH_3PbI_3$/spiro-OMeTAD/Ag	21.38	1,160	0.72	17.76	Hole blocking layer, reduced trap site density atop TiO_2	[167]
ITO/PEDOT:PSS/$CH_3NH_3Pb_{3-x}Cl_x$/PCBM/DMAPA-C_{60}/Ag	17.9	970	0.77	13.4	Formation of a dipole layer and a better surface film coverage	[124]
ITO/PEDOT:PSS/perovskite/PCBM/C_{60}-N/Ag	18.95 ± 1.06	980 ± 30	0.70 ± 0.03	13.00 ± 1.04	Enhancing electron extraction, prolonging free carrier lifetime, decreasing work function at the interface	[125]
FTO/TiO_2/$CH_3NH_3PbI_3$/GO/spiro-OMeTAD/Au	20.2	1,040	0.73	15.1	Improving contact, retarding charge recombination	[128]
FTO/c-TiO_2/mp-TiO_2/GO-Li/$CH_3NH_3PbI_3$/spiro-OMeTAD/Au	19.61	859	0.70	11.8	Enhancing electron injection, passivating oxygen vacancies/defects of mp-TiO_2	[129]
ITO/PEDOT:PSS/GO:NH_3/$CH_3NH_3PbI_{3-x}Cl_x$/PCBM/sBphen/Ag	21.27 ± 0.55	1,020 ± 10	0.72 ± 0.01	15.90 ± 0.17	Improving crystallization and orientation order of perovskite, enhancing absorption, better matched energy-level-alignment	[130]
FTO/TiO_2/Al_2O_3+$CH_3NH_3PbI_{3-x}Cl_x$/P3HT-SWNTs/spiro-OMeTAD/Ag	21.4	1,020	0.71	15.4	Enhancing charge extraction through undoped spiro-OMeTAD	[132]
FTO/c-TiO_2/$CH_3NH_3PbI_3$/s-SWCNT/spiro-OMeTAD/Ag	20.8 ± 0.3	1,070 ± 9	0.73 ± 0.02	16.1 ± 0.3	Tracking charge extraction and recombination, enabling long-lived charge separation	[168]
FTO/TiO_2/rGS/$CH_3NH_3PbI_3$/spiro-OMeTAD/Au	22.8 ± 0.9	1,050 ± 30	0.72 ± 0.02	16.2 ± 1	Improving carrier transportation, amending stability and hysteresis	[169]
FTO/c-TiO_2/mp-Al_2O_3/$CH_3NH_3PbI_{3-x}C_{lx}$/IPFB/spiro-OMeTAD/Ag	23.38	1,060	0.67	15.7	Passivating trap states at perovskite surface	[170]
FTO/c-TiO_2/mp-TiO_2/HOCO–R–$NH^{3+}I^-$/$CH_3NH_3PbI_3$/spiro-OMeTAD/Ag/Au	19.2	1,000	0.62	12.0	Retarding charge recombination, passivating surface traps of porous titania, promoting electron injection	[136]
FTO/TiO_2/$CH_3NH_3PbI_3$/C_{12}-silane/spiro-OMeTAD/Ag	20.23	959	0.68	13.74	Blocking electron recombination and resisting moisture	[140]
ITO/PEDOT:PSS/$CH_3NH_3PbI_3$/PCBM/MUTAB/Ag	20.66 ± 0.75	1,020 ± 10	0.74 ± 0.03	15.50 ± 0.42	Covalent Ag–S bonds decrease contact resistance, inducing a favorable interfacial dipole to lower work function of Ag	[171]
FTO/TiO_2/silane/(ZrO_2+$CH_3NH_3PbI_3$)/C	19.6	833	0.72	12.7	Tuning the interface electronic structure, passivate recombination	[135]
ITO/ZnO/C3-SAM/$CH_3NH_3PbI_3$/spiro-OMeTAD/MoO_3/Ag	22.51	1,070	0.65	15.67	$CH_3NH_3PbI_3$ with reduced pinholes and trap states density, forming permanent dipole moment	[134]
FTO/TiO_2/glycine/$CH_3NH_3PbI_3$/spiro-OMeTAD/Au	16.20 ± 2.31	980 ± 20	0.60 ± 0.05	9.48 ± 1.40	Higher coverage of $CH_3NH_3PbI_3$ crystals on TiO_2 surface	[137]
FTO/TiO_2/HOOC–Ph–SH/$CH_3NH_3PbI_3$/HS-PhF5/spiro-OMeTAD/Au	20.66	1,020	0.67	14.1	HOOC–Ph–SH facilitates electron transfer and alters mophology of perovskite crystal growth; HS-PhF5 enhances stability	[138]
FTO/c-TiO_2/$CH_3NH_3PbI_3$/TEA/spiro-OMeTAD/Ag	20.4	995	0.74	15.02	Enhanced surface hydrophobicity, superior moisture stability	[139]

(Continued)

Device structure	J_{sc} (mA/cm^2)	V_{oc} (mV)	FF	PCE (%)	Remarks	Ref.
FTO/c-TiO_2/mp-TiO_2/$CH_3NH_3PbI_{3-x}Cl_x$/H_2N–$(CH_2)_3$–$Si(OC_2H_5)_3$/spiro-OMeTAD/Ag	16.55	902	0.73	11.8	Changing chemical composition of perovskite surface	[172]
FTO/NiO/DEA/$CH_3NH_3PbI_{3-x}Cl_x$/PCBM/PN_4N/Ag	20.90	950	0.80	15.90	Enhancing perovskite crystallization and improving interface contact	[173]
ITO/PEDOT:PSS/$CH_3NH_3PbI_3$/PCBM/BCP/Al	10.32	600	0.63	3.9	Hole-blocking layer	[142]
ITO/PEDOT:PSS/$CH_3NH_3PbI_3$/ICBA/C_{60}/BCP/Al	15.7	970	0.80	12.2	Avoiding leakage, passivating traps in $CH_3NH_3PbI_3$	[143]
ITO/PEDOT:PSS/$CH_3NH_3PbI_{3-x}Cl_x$/PCBM/PDINO/Ag	18.8	950	0.79	14.0	Improving contact, reducing series resistance (R_s)	[144]
ITO/(PEDOT:PSS+Ag NPs)/$CH_3NH_3PbI_{3-x}Cl_x$/PCBM/sBphen/Ag	21.51	930	0.79	15.75	Ag-NPs improve the electrical property of PEDOT:PSS; sBphen modifies the surface morphology by filling the voids	[145]
ITO/PEDOT:PSS/$CH_3NH_3PbI_{3-x}Cl_x$/PCBM/Rhodamine 101/LiF/Ag	17.72 ± 0.37	1,010 ± 10	0.73 ± 0.02	13.1	Lowering work function of electrodes	[146]
ITO/PEDOT:PSS/$MAPbI_{3-x}Br_x$/PCBM/sBCP/Ag	17.07	890	0.85	13.06	Reducing leakage current and charge transfer resistance	[148]
ITO/PEDOT:PSS/$CH_3NH_3PbI_{3-x}Cl_x$/PCBM/Bphen-$Ir(MDQ)_2(acac)$/Ag	21.89	950	0.75	15.87	Facilitating interface contact and electron extraction	[147]
FTO/TiO_2/$CH_3NH_3PbI_3$/TPB/Au	13.26 ± 0.51	810 ± 31	0.58 ± 0.02	6.26 ± 0.40	Increasing interfacial resistance of $CH_3NH_3PbI_3$/Au interface and retarding electron recombination process	[174]
ITO/PEDOT:PSS/$CH_3NH_3PbCl_xI_{3-x}$/PCBM/PN_4N/Al	20.61	1,000	0.73	15.0	Reducing contact resistance, suppressing bimolecular recombination and improving electron transport	[151]
ITO/PEDOT:PSS/$CH_3NH_3PbI_{3-x}Cl_x$/PCBM/PEIE/Ag	17.32 ± 0.31	899 ± 1	0.77 ± 0.01	12.01	Reducing work function of metal electrode	[150]
ITO/PEDOT:PSS/$CH_3NH_3PbI_{3-x}Cl_x$/PCBM/P3TMAHT/Ag	17.10 ± 0.42	899 ± 1	0.74 ± 0.01	11.28	Reducing work function of metal electrode	[150]
ITO/PEIE/Y:TiO_2/perovskite/spiro-OMeTAD/Au	22.80	1,150	0.76	19.3	Reducing work function of ITO	[78]
ITO/PEDOT:PSS/$CH_3NH_3PbI_3$/LiSPS/PCBM/Al	20.90	850	0.78	13.83	Optimized contact, reduced leakage current	[153]
ITO/PFN-OX:ZnO/$CH_3NH_3PbI_3$/spiro-OMeTAD/Au	20.7	1,030	0.76	16.2	Efficient electron extraction and hole blocking	[175]
FTO/TiO_x/PEO/$CH_3NH_3PbI_xCl_{3-x}$/spiro-OMeTAD/Au	19.0 ± 0.8	1,050 ± 30	0.62 ± 0.02	12.3 ± 0.64	Retarding back recombination and enhance electron collection	[176]
FTO/c-TiO_2/(TiO_2+$CH_3NH_3PbI_3$)/PEI/spiro-OMeTAD/Au	18.30	1,000	0.74	13.48	Reducing moisture intrusion and increase adhesion at the interface	[177]
ITO/PTAA:F_4-TCNQ/$CH_3NH_3PbI_3$/insulating polymer/C_{60}/BCP/Al	22.9	1,100	0.81	20.3	Reducing charge recombination	[154]
ITO/PEDOT:PSS/$CH_3NH_3PbI_3$/PCBM/PEOz nanodots/Ag	20.5	910	0.77	14.52	Minimizing contact barrier and reducing work function of Ag	[152]
FTO/TiO_2/graphene QDs/$CH_3NH_3PbI_3$/spiro-OMeTAD/Au	17.06	937	0.64	10.15	Facilitating electron extraction	[155]
FTO/c-TiO_2/$CH_3NH_3PbI_3$/$CH_3NH_3PbBr_{3-x}I_x$ QDs/spiro-OMeTAD/Au	19.51	948	0.72	13.32	Facilitating hole extraction	[157]

from water while transferring electrons to the outer Pt hydrogen-evolution catalyst. Recently, an ultrathin Ni layer and a CNT/polymer composite layer were developed to function together for the perovskite-integrated photoelectrolysis of water [180]. These findings will spur further attempts to greatly enhance the stability of perovskite materials towards the ultimate goal of harnessing solar power. With a deeper understanding of the interface and the exploration of novel interfacial tailoring approaches, interface engineering is expected to drive further developments of PSCs.

Another goal for PSCs is to make them ubiquitous in everyday life; thus, flexible and efficient PSCs are in urgent demand. p–i–n inverted planar PSCs are more promising than n–i–p planar PSCs and mesoscopic PSCs, considering their cost-effective manufacturing. The relatively unstable PEDOT:PSS and rather expensive fullerene ETL can be optimized by interfacial engineering to enhance the device performance.

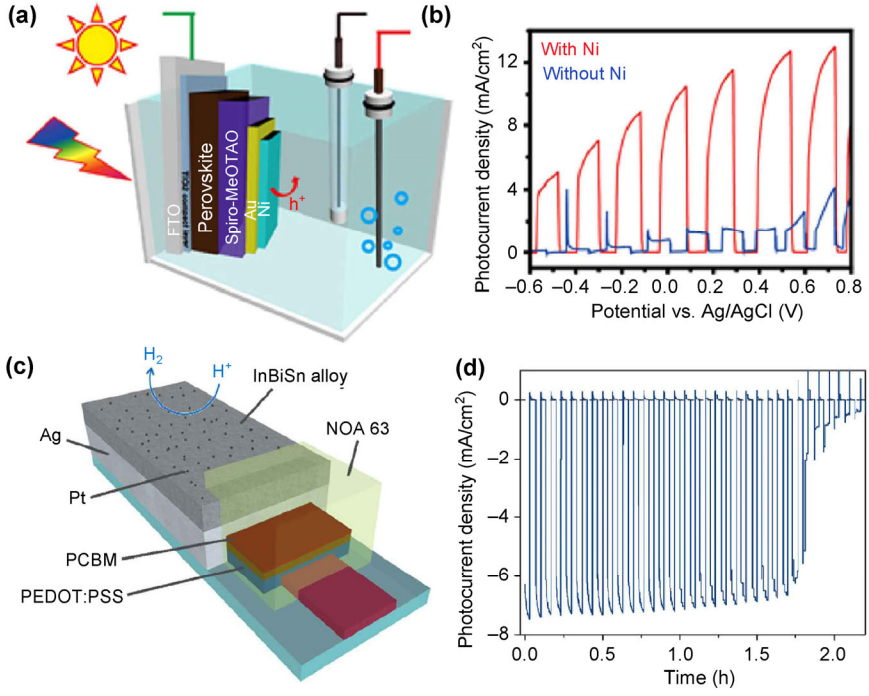

Figure 11 Illustration of a perovskite photoanode and photocathode for solar-driven hydrogen evolution. (a) and (b) Schematic and performance of the photoelectrochemical application of a Ni-encapsulated planar heterojunction perovskite photoanode in a standard PEC cell. Reproduced with permission from Ref. [178], © American Chemical Society 2015. (c) and (d) Configuration and stability of an inverted-planar heterojunction PSC-based photocathode. An InBiSn alloy was applied for encapsulation. Reproduced with permission from Ref. [179], © Nature Publishing Group 2016.

Acknowledgements

The authors thank the following funding agencies for supporting this work: the National Basic Research Program of China (No. 2013CB934104), the National Natural Science Foundation of China (Nos. 21322311 and 21473038), the Science and Technology Commission of Shanghai Municipality (No. 14JC1490500), the Program for Professor of Special Appointment (Eastern Scholar) at Shanghai Institutions of Higher Learning, and the Collaborative Innovation Center of Chemistry for Energy Materials (2011-iChem).

References

[1] Kojima, A.; Teshima, K.; Shirai, Y.; Miyasaka, T. Organometal halide perovskites as visible-light sensitizers for photovoltaic cells. *J. Am. Chem. Soc.* **2009**, *131*, 6050–6051.

[2] National renewable energy laboratory. Photovoltaic Research. www.nrel.gov/ncpv/images/efficiency_chart.jpg (accessed Oct 25, 2016).

[3] Niu, G. D.; Li, W. Z.; Li, J. W.; Wang, L. D. Progress of interface engineering in perovskite solar cells. *Sci. China Mater.* **2016**, *59*, 728–742.

[4] Sha, W. E. I.; Ren, X. G.; Chen, L. Z.; Choy, W. C. H. The efficiency limit of $CH_3NH_3PbI_3$ perovskite solar cells. *Appl. Phys. Lett.* **2015**, *106*, 221104.

[5] Tiep, N. H.; Ku, Z. L.; Fan, H. J. Recent advances in improving the stability of perovskite solar cells. *Adv. Energy Mater.* **2016**, *6*, 1501420.

[6] Guerrero, A.; You, J. B.; Aranda, C.; Kang, Y. S.; Garcia-Belmonte, G.; Zhou, H. P.; Bisquert, J.; Yang, Y. Interfacial degradation of planar lead halide perovskite solar cells. *ACS Nano* **2016**, *10*, 218–224.

[7] Manser, J. S.; Kamat, P. V. Band filling with free charge carriers in organometal halide perovskites. *Nat. Photonics* **2014**, *8*, 737–743.

[8] Yamada, Y.; Nakamura, T.; Endo, M.; Wakamiya, A.; Kanemitsu, Y. Photocarrier recombination dynamics in perovskite $CH_3NH_3PbI_3$ for solar cell applications. *J. Am. Chem. Soc.* **2014**, *136*, 11610–11613.

[9] D'Innocenzo, V.; Grancini, G.; Alcocer, M. J. P.; Kandada, A. R. S.; Stranks, S. D.; Lee, M. M.; Lanzani, G.; Snaith, H. J.; Petrozza, A. Excitons versus free charges in organo-lead

tri-halide perovskites. *Nat. Commun.* **2014**, *5*, 3586.

[10] Edri, E.; Kirmayer, S.; Mukhopadhyay, S.; Gartsman, K.; Hodes, G.; Cahen, D. Elucidating the charge carrier separation and working mechanism of $CH_3NH_3PbI_{3-x}Cl_x$ perovskite solar cells. *Nat. Commun.* **2014**, *5*, 3461.

[11] Sharma, B. L.; Purohit, R. K. *Semiconductor Heterojunctions*; Elsevier: New York, 2015.

[12] Shi, J. J.; Xu, X.; Li, D. M.; Meng, Q. B. Interfaces in perovskite solar cells. *Small* **2015**, *11*, 2472–2486.

[13] Sze, S. M.; Ng, K. K. *Physics of Semiconductor Devices*, 3rd ed.; John Wiley & Sons: Hoboken, New Jersey, 2006.

[14] Lindblad, R.; Bi, D. Q.; Park, B.-W.; Oscarsson, J.; Gorgoi, M.; Siegbahn, H.; Odelius, M.; Johansson, E. M.; Rensmo, H. K. Electronic structure of $TiO_2/CH_3NH_3PbI_3$ perovskite solar cell interfaces. *J. Phys. Chem. Lett.* **2014**, *5*, 648–653.

[15] Schulz, P.; Edri, E.; Kirmayer, S.; Hodes, G.; Cahen, D.; Kahn, A. Interface energetics in organo-metal halide perovskite-based photovoltaic cells. *Energy Environ. Sci.* **2014**, *7*, 1377–1381.

[16] Miller, E. M.; Zhao, Y. X.; Mercado, C. C.; Saha, S. K.; Luther, J. M.; Zhu, K.; Stevanović, V.; Perkins, C. L.; van de Lagemaat, J. Substrate-controlled band positions in $CH_3NH_3PbI_3$ perovskite films. *Phys. Chem. Chem. Phys.* **2014**, *16*, 22122–22130.

[17] Jiang, Q. L.; Sheng, X.; Shi, B.; Feng, X. J.; Xu, T. Nickel-cathoded perovskite solar cells. *J. Phys. Chem. C* **2014**, *118*, 25878–25883.

[18] Jeong, I.; Kim, H. J.; Lee, B.-S.; Son, H. J.; Kim, J. Y.; Lee, D.-K.; Kim, D.-E.; Lee, J.; Ko, M. J. Highly efficient perovskite solar cells based on mechanically durable molybdenum cathode. *Nano Energy* **2015**, *17*, 131–139.

[19] Jiang, Z. Y.; Chen, X. H.; Lin, X. H.; Jia, X. K.; Wang, J. F.; Pan, L. K.; Huang, S. M.; Zhu, F. R.; Sun, Z. Amazing stable open-circuit voltage in perovskite solar cells using AgAl alloy electrode. *Sol. Energ. Mat. Sol. C* **2016**, *146*, 35–43.

[20] Ku, Z. L.; Xia, X. H.; Shen, H.; Tiep, N. H.; Fan, H. J. A mesoporous nickel counter electrode for printable and reusable perovskite solar cells. *Nanoscale* **2015**, *7*, 13363–13368.

[21] Deng, Q. R.; Li, Y. Q.; Chen, L.; Wang, S. G.; Wang, G. M.; Sheng, Y. L.; Shao, G. S. The effects of electron and hole transport layer with the electrode work function on perovskite solar cells. *Mod. Phys. Lett. B* **2016**, *30*, 1650341.

[22] Wei, Z. H.; Chen, H. N.; Yan, K. Y.; Yang, S. H. Inkjet printing and instant chemical transformation of a $CH_3NH_3PbI_3$/nanocarbon electrode and interface for planar perovskite solar cells. *Angew. Chem., Int. Ed.* **2014**, *53*, 13239–13243.

[23] Mei, A. Y.; Li, X.; Liu, L. F.; Ku, Z. L.; Liu, T. F.; Rong, Y. G.; Xu, M.; Hu, M.; Chen, J. Z.; Yang, Y. et al. A hole-conductor–free, fully printable mesoscopic perovskite solar cell with high stability. *Science* **2014**, *345*, 295–298.

[24] Wei, Z. H.; Yan, K. Y.; Chen, H. N.; Yi, Y.; Zhang, T.; Long, X.; Li, J. K.; Zhang, L. X.; Wang, J. N.; Yang, S. H. Cost-efficient clamping solar cells using candle soot for hole extraction from ambipolar perovskites. *Energy Environ. Sci.* **2014**, *7*, 3326–3333.

[25] Ku, Z. L.; Rong, Y. G.; Xu, M.; Liu, T. F.; Han, H. W. Full printable processed mesoscopic $CH_3NH_3PbI_3/TiO_2$ heterojunction solar cells with carbon counter electrode. *Sci. Rep.* **2013**, *3*, 3132.

[26] Liu, D. Y.; Yang, J. L.; Kelly, T. L. Compact layer free perovskite solar cells with 13.5% efficiency. *J. Am. Chem. Soc.* **2014**, *136*, 17116–17122.

[27] Etgar, L.; Gao, P.; Xue, Z. S.; Peng, Q.; Chandiran, A. K.; Liu, B.; Nazeeruddin, M. K.; Grätzel, M. Mesoscopic $CH_3NH_3PbI_3/TiO_2$ heterojunction solar cells. *J. Am. Chem. Soc.* **2012**, *134*, 17396–17399.

[28] Yang, B.; Dyck, O.; Poplawsky, J.; Keum, J.; Puretzky, A.; Das, S.; Ivanov, I.; Rouleau, C.; Duscher, G.; Geohegan, D. et al. Perovskite solar cells with near 100% internal quantum efficiency based on large single crystalline grains and vertical bulk heterojunctions. *J. Am. Chem. Soc.* **2015**, *137*, 9210–9213.

[29] Shao, Y. C.; Fang, Y. J.; Li, T.; Wang, Q.; Dong, Q. F.; Deng, Y. H.; Yuan, Y. B.; Wei, H. T.; Wang, M. Y.; Gruverman, A. et al. Grain boundary dominated ion migration in polycrystalline organic–inorganic halide perovskite films. *Energy Environ. Sci.* **2016**, *9*, 1752–1759.

[30] Leguy, A. l. M.; Hu, Y. H.; Campoy-Quiles, M.; Alonso, M. I.; Weber, O. J.; Azarhoosh, P.; Van Schilfgaarde, M.; Weller, M. T.; Bein, T.; Nelson, J. et al. Reversible hydration of $CH_3NH_3PbI_3$ in films, single crystals, and solar cells. *Chem. Mater.* **2015**, *27*, 3397–3407.

[31] Boopathi, K. M.; Mohan, R.; Huang, T.-Y.; Budiawan, W.; Lin, M.-Y.; Lee, C.-H.; Ho, K.-C.; Chu, C.-W. Synergistic improvements in stability and performance of lead iodide perovskite solar cells incorporating salt additives. *J. Mater. Chem. A* **2016**, *4*, 1591–1597.

[32] Liang, P. W.; Liao, C. Y.; Chueh, C. C.; Zuo, F.; Williams, S. T.; Xin, X. K.; Lin, J.; Jen, A. K. Y. Additive enhanced crystallization of solution-processed perovskite for highly efficient planar-heterojunction solar cells. *Adv. Mater.* **2014**, *26*, 3748–3754.

[33] Wang, K.; Liu, C.; Du, P. C.; Zheng, J.; Gong, X. Bulk heterojunction perovskite hybrid solar cells with large fill factor. *Energy Environ. Sci.* **2015**, *8*, 1245–1255.

[34] Chiang, C.-H.; Wu, C.-G. Bulk heterojunction perovskite-PCBM solar cells with high fill factor. *Nat. Photonics* **2016**,

10, 196–200.

[35] Wu, Y. Z.; Yang, X. D.; Chen, W.; Yue, Y. F.; Cai, M. L.; Xie, F. X.; Bi, E. B.; Islam, A.; Han, L. Y. Perovskite solar cells with 18.21% efficiency and area over 1 cm^2 fabricated by heterojunction engineering. *Nat. Energy* **2016**, *1*, 16148.

[36] Zhao, Y. C.; Wei, J.; Li, H.; Yan, Y.; Zhou, W. K.; Yu, D. P.; Zhao, Q. A polymer scaffold for self-healing perovskite solar cells. *Nat. Commun.* **2016**, *7*, 10228.

[37] Bi, D. Q.; Yi, C. Y.; Luo, J. S.; Décoppet, J.-D.; Zhang, F.; Zakeeruddin, S. M.; Li, X.; Hagfeldt, A.; Grätzel, M. Polymer-templated nucleation and crystal growth of perovskite films for solar cells with efficiency greater than 21%. *Nat. Energy* **2016**, *1*, 16142.

[38] Chuang, P.-Y.; Chuang, C.-N.; Yu, C.-C.; Wang, L.-Y.; Hsieh, K.-H. Enhance the stability and efficiency of perovskite solar cell via gel-type polyurethane. *Polymer* **2016**, *97*, 196–204.

[39] Li, X.; Dar, M. I.; Yi, C. Y.; Luo, J. S.; Tschumi, M.; Zakeeruddin, S. M.; Nazeeruddin, M. K.; Han, H. W.; Grätzel, M. Improved performance and stability of perovskite solar cells by crystal crosslinking with alkylphosphonic acid ω-ammonium chlorides. *Nat. Chem.* **2015**, *7*, 703–711.

[40] Pellet, N.; Gao, P.; Gregori, G.; Yang, T. Y.; Nazeeruddin, M. K.; Maier, J.; Grätzel, M. Mixed-organic-cation perovskite photovoltaics for enhanced solar-light harvesting. *Angew. Chem., Int. Ed.* **2014**, *53*, 3151–3157.

[41] Smith, I. C.; Hoke, E. T.; Solis-Ibarra, D.; McGehee, M. D.; Karunadasa, H. I. A layered hybrid perovskite solar-cell absorber with enhanced moisture stability. *Angew. Chem.* **2014**, *126*, 11414–11417.

[42] Jeon, N. J.; Noh, J. H.; Yang, W. S.; Kim, Y. C.; Ryu, S.; Seo, J.; Seok, S. I. Compositional engineering of perovskite materials for high-performance solar cells. *Nature* **2015**, *517*, 476–480.

[43] Hu, Y. H.; Schlipf, J.; Wussler, M.; Petrus, M. L.; Jaegermann, W.; Bein, T.; Müller-Buschbaum, P.; Docampo, P. Hybrid perovskite/perovskite heterojunction solar cells. *ACS Nano* **2016**, *10*, 5999–6007.

[44] Seol, D. J.; Lee, J. W.; Park, N. G. On the role of interfaces in planar-structured $HC(NH_2)_2PbI_3$ perovskite solar cells. *ChemSusChem* **2015**, *8*, 2414–2419.

[45] Yang, W. S.; Noh, J. H.; Jeon, N. J.; Kim, Y. C.; Ryu, S.; Seo, J.; Seok, S. I. High-performance photovoltaic perovskite layers fabricated through intramolecular exchange. *Science* **2015**, *348*, 1234–1237.

[46] Colella, S.; Mosconi, E.; Pellegrino, G.; Alberti, A.; Guerra, V. L. P.; Masi, S.; Listorti, A.; Rizzo, A.; Condorelli, G. G.; De Angelis, F. et al. Elusive presence of chloride in mixed halide perovskite solar cells. *J. Phys. Chem. Lett.* **2014**, *5*, 3532–3538.

[47] Mosconi, E.; Ronca, E.; De Angelis, F. First-principles investigation of the TiO_2/organohalide perovskites interface: The role of interfacial chlorine. *J. Phys. Chem. Lett.* **2014**, *5*, 2619–2625.

[48] Liang, P. W.; Chueh, C. C.; Xin, X. K.; Zuo, F.; Williams, S. T.; Liao, C. Y.; Jen, A. K. Y. High-performance planar-heterojunction solar cells based on ternary halide large-band-gap perovskites. *Adv. Energy Mater.* **2015**, *5*, 1400960.

[49] Pellegrino, G.; Colella, S.; Deretzis, I.; Condorelli, G. G.; Smecca, E.; Gigli, G.; La Magna, A.; Alberti, A. Texture of $MAPbI_3$ layers assisted by chloride on flat TiO_2 substrates. *J. Phys. Chem. C* **2015**, *119*, 19808–19816.

[50] Cojocaru, L.; Uchida, S.; Matsubara, D.; Matsumoto, H.; Ito, K.; Otsu, Y.; Chapon, P.; Nakazaki, J.; Kubo, T.; Segawa, H. Direct confirmation of distribution for Cl^- in $CH_3NH_3PbI_{3-x}Cl_x$ layer of perovskite solar cells. *Chem. Lett.* **2016**, *45*, 884–886.

[51] Yang, M. J.; Zhang, T. Y.; Schulz, P.; Li, Z.; Li, G.; Kim, D. H.; Guo, N. J.; Berry, J. J.; Zhu, K.; Zhao, Y. X. Facile fabrication of large-grain $CH_3NH_3PbI_{3-x}Br_x$ films for high-efficiency solar cells via CH_3NH_3Br-selective Ostwald ripening. *Nat. Commun.* **2016**, *7*, 12305.

[52] Luo, P. F.; Liu, Z. F.; Xia, W.; Yuan, C. C.; Cheng, J. G.; Xu, C. X.; Lu, Y. W. Chlorine-conducted defect repairment and seed crystal-mediated vapor growth process for controllable preparation of efficient and stable perovskite solar cells. *J. Mater. Chem. A* **2015**, *3*, 22949–22959.

[53] Liu, D.; Wu, L. L.; Li, C. X.; Ren, S. Q.; Zhang, J. Q.; Li, W.; Feng, L. H. Controlling $CH_3NH_3PbI_{3-x}Cl_x$ film morphology with two-step annealing method for efficient hybrid perovskite solar cells. *ACS Appl. Mater. Interfaces* **2015**, *7*, 16330–16337.

[54] Zhu, W. D.; Yu, T.; Li, F. M.; Bao, C. X.; Gao, H.; Yi, Y.; Yang, J.; Fu, G.; Zhou, X. X.; Zou, Z. G. A facile, solvent vapor–fumigation-induced, self-repair recrystallization of $CH_3NH_3PbI_3$ films for high-performance perovskite solar cells. *Nanoscale* **2015**, *7*, 5427–5434.

[55] Xiao, M. D.; Huang, F. Z.; Huang, W. C.; Dkhissi, Y.; Zhu, Y.; Etheridge, J.; Gray-Weale, A.; Bach, U.; Cheng, Y. B.; Spiccia, L. A fast deposition-crystallization procedure for highly efficient lead iodide perovskite thin-film solar cells. *Angew. Chem.* **2014**, *126*, 10056–10061.

[56] Cao, J.; Jing, X. J.; Yan, J. Z.; Hu, C. Y.; Chen, R. H.; Yin, J.; Li, J.; Zheng, N. F. Identifying the molecular structures of intermediates for optimizing the fabrication of high-quality perovskite films. *J. Am. Chem. Soc.* **2016**, *138*, 9919–9926.

[57] Kim, H.-B.; Choi, H.; Jeong, J.; Kim, S.; Walker, B.; Song, S.; Kim, J. Y. Mixed solvents for the optimization of morphology in solution-processed, inverted-type perovskite/fullerene hybrid solar cells. *Nanoscale* **2014**, *6*, 6679–6683.

[58] Wu, Y. Z.; Islam, A.; Yang, X. D.; Qin, C. J.; Liu, J.; Zhang, K.; Peng, W. Q.; Han, L. Y. Retarding the crystallization of PbI_2 for highly reproducible planar-structured perovskite solar cells via sequential deposition. *Energy Environ. Sci.* **2014**, *7*, 2934–2938.

[59] Jeon, N. J.; Noh, J. H.; Kim, Y. C.; Yang, W. S.; Ryu, S.; Seok, S. I. Solvent engineering for high-performance inorganic–organic hybrid perovskite solar cells. *Nat. Mater.* **2014**, *13*, 897–903.

[60] Jung, J. W.; Williams, S. T.; Jen, A. K.-Y. Low-temperature processed high-performance flexible perovskite solar cells via rationally optimized solvent washing treatments. *RSC Adv.* **2014**, *4*, 62971–62977.

[61] Lin, N.; Qiao, J.; Dong, H. P.; Ma, F. S.; Wang, L. D. Morphology-controlled $CH_3NH_3PbI_3$ films by hexane-assisted one-step solution deposition for hybrid perovskite mesoscopic solar cells with high reproductivity. *J. Mater. Chem. A* **2015**, *3*, 22839–22845.

[62] Hao, F.; Stoumpos, C. C.; Liu, Z.; Chang, R. P. H.; Kanatzidis, M. G. Controllable perovskite crystallization at a gas–solid interface for hole conductor-free solar cells with steady power conversion efficiency over 10%. *J. Am. Chem. Soc.* **2014**, *136*, 16411–16419.

[63] Tai, Q. D.; You, P.; Sang, H. Q.; Liu, Z. K.; Hu, C. L.; Chan, H. L. W.; Yan, F. Efficient and stable perovskite solar cells prepared in ambient air irrespective of the humidity. *Nat. Commun.* **2016**, *7*, 11105.

[64] Xia, X.; Li, H. C.; Wu, W. Y.; Li, Y. H.; Fei, D. H.; Gao, C. X.; Liu, X. Z. Efficient light harvester layer prepared by solid/mist interface reaction for perovskite solar cells. *ACS Appl. Mater. Interfaces* **2015**, *7*, 16907–16912.

[65] Xiao, Z. G.; Bi, C.; Shao, Y. C.; Dong, Q. F.; Wang, Q.; Yuan, Y. B.; Wang, C. G.; Gao, Y. L.; Huang, J. S. Efficient, high yield perovskite photovoltaic devices grown by interdiffusion of solution-processed precursor stacking layers. *Energy Environ. Sci.* **2014**, *7*, 2619–2623.

[66] Xie, Y.; Shao, F.; Wang, Y. M.; Xu, T.; Wang, D. L.; Huang, F. Q. Enhanced performance of perovskite $CH_3NH_3PbI_3$ solar cell by using CH_3NH_3I as additive in sequential deposition. *ACS Appl. Mater. Interfaces* **2015**, *7*, 12937–12942.

[67] Das, S.; Yang, B.; Gu, G.; Joshi, P. C.; Ivanov, I. N.; Rouleau, C. M.; Aytug, T.; Geohegan, D. B.; Xiao, K. High-performance flexible perovskite solar cells by using a combination of ultrasonic spray-coating and low thermal budget photonic curing. *ACS Photonics* **2015**, *2*, 680–686.

[68] Yang, L. J.; Wang, J. C.; Leung, W. W.-F. Lead iodide thin film crystallization control for high-performance and stable solution-processed perovskite solar cells. *ACS Appl. Mater. Interfaces* **2015**, *7*, 14614–14619.

[69] Chen, H. N.; Wei, Z. H.; Zheng, X. L.; Yang, S. H. A scalable electrodeposition route to the low-cost, versatile and controllable fabrication of perovskite solar cells. *Nano Energy* **2015**, *15*, 216–226.

[70] Ying, C.; Shi, C. W.; Wu, N.; Zhang, J. C.; Wang, M. A two-layer structured PbI_2 thin film for efficient planar perovskite solar cells. *Nanoscale* **2015**, *7*, 12092–12095.

[71] Singh, T.; Miyasaka, T. High performance perovskite solar cell via multi-cycle low temperature processing of lead acetate precursor solutions. *Chem. Commun.* **2016**, *52*, 4784–4787.

[72] Stoumpos, C. C.; Malliakas, C. D.; Kanatzidis, M. G. Semiconducting tin and lead iodide perovskites with organic cations: Phase transitions, high mobilities, and near-infrared photoluminescent properties. *Inorg. Chem.* **2013**, *52*, 9019–9038.

[73] Li, C.; Lu, X.; Ding, W.; Feng, L.; Gao, Y.; Guo, Z. Formability of ABX_3 (X = F, Cl, Br, I) halide perovskites. *Acta Cryst.* **2008**, *64*, 702–707.

[74] Supasai, T.; Rujisamphan, N.; Ullrich, K.; Chemseddine, A.; Dittrich, T. Formation of a passivating $CH_3NH_3PbI_3/PbI_2$ interface during moderate heating of $CH_3NH_3PbI_3$ layers. *Appl. Phys. Lett.* **2013**, *103*, 183906.

[75] Cao, D. H.; Stoumpos, C. C.; Malliakas, C. D.; Katz, M. J.; Farha, O. K.; Hupp, J. T.; Kanatzidis, M. G. Remnant PbI_2, an unforeseen necessity in high-efficiency hybrid perovskite-based solar cells? *APL Mater.* **2014**, *2*, 091101.

[76] Roldán-Carmona, C.; Gratia, P.; Zimmermann, I.; Grancini, G.; Gao, P.; Graetzel, M.; Nazeeruddin, M. K. High efficiency methylammonium lead triiodide perovskite solar cells: The relevance of non-stoichiometric precursors. *Energy Environ. Sci.* **2015**, *8*, 3550–3556.

[77] Wu, W.-Q.; Huang, F. Z.; Chen, D. H.; Cheng, Y.-B.; Caruso, R. A. Solvent-mediated dimension tuning of semiconducting oxide nanostructures as efficient charge extraction thin films for perovskite solar cells with efficiency exceeding 16%. *Adv. Energy Mater.* **2016**, *6*, 1502027.

[78] Zhou, H. P.; Chen, Q.; Li, G.; Luo, S.; Song, T.-B.; Duan, H.-S.; Hong, Z. R.; You, J. B.; Liu, Y. S.; Yang, Y. Interface engineering of highly efficient perovskite solar cells. *Science* **2014**, *345*, 542–546.

[79] Chen, W.; Wu, Y. Z.; Yue, Y. F.; Liu, J.; Zhang, W. J.; Yang, X. D.; Chen, H.; Bi, E. B.; Ashraful, I.; Grätzel, M. et al. Efficient and stable large-area perovskite solar cells with inorganic charge extraction layers. *Science* **2015**, *350*, 944–948.

[80] Gubbala, S.; Chakrapani, V.; Kumar, V.; Sunkara, M. K. Band-edge engineered hybrid structures for dye-sensitized solar cells based on SnO_2 nanowires. *Adv. Funct. Mater.* **2008**, *18*, 2411–2418.

[81] Tao, H.; Ke, W. J.; Wang, J.; Liu, Q.; Wan, J. W.; Yang, G.; Fang, G. J. Perovskite solar cell based on network nanoporous layer consisted of TiO_2 nanowires and its interface optimization. *J. Power. Sources* **2015**, *290*, 144–152.

[82] Chen, H. N.; Wei, Z. H.; Yan, K. Y.; Yi, Y.; Wang, J. N.; Yang, S. H. Liquid phase deposition of TiO_2 nanolayer affords $CH_3NH3PbI_3$/nanocarbon solar cells with high open-circuit voltage. *Faraday Discuss* **2014**, *176*, 271–286.

[83] Wang, H.-H.; Chen, Q.; Zhou, H. P.; Song, L.; St Louis, Z.; De Marco, N.; Fang, Y. H.; Sun, P. Y.; Song, T.-B.; Chen, H. J. et al. Improving the TiO_2 electron transport layer in perovskite solar cells using acetylacetonate-based additives. *J. Mater. Chem. A* **2015**, *3*, 9108–9115.

[84] Zhang, J.; Pauporté, T. Effects of oxide contact layer on the preparation and properties of $CH_3NH_3PbI_3$ for perovskite solar cell application. *J. Phys. Chem. C* **2015**, *119*, 14919–14928.

[85] Baena, J. P. C.; Steier, L.; Tress, W.; Saliba, M.; Neutzner, S.; Matsui, T.; Giordano, F.; Jacobsson, T. J.; Kandada, A. R. S.; Zakeeruddin, S. M. et al. Highly efficient planar perovskite solar cells through band alignment engineering. *Energy Environ. Sci.* **2015**, *8*, 2928–2934.

[86] Song, J. X.; Zheng, E. Q.; Bian, J.; Wang, X.-F.; Tian, W. J.; Sanehira, Y.; Miyasaka, T. Low-temperature SnO_2-based electron selective contact for efficient and stable perovskite solar cells. *J. Mater. Chem. A* **2015**, *3*, 10837–10844.

[87] Mahmood, K.; Swain, B. S.; Kirmani, A. R.; Amassian, A. Highly efficient perovskite solar cells based on a nano-structured WO_3–TiO_2 core–shell electron transporting material. *J. Mater. Chem. A* **2015**, *3*, 9051–9057.

[88] Liu, J.; Gao, C.; Luo, L. Z.; Ye, Q. Y.; He, X. L.; Ouyang, L. Q.; Guo, X. W.; Zhuang, D. M.; Liao, C.; Mei, J. et al. Low-temperature, solution processed metal sulfide as an electron transport layer for efficient planar perovskite solar cells. *J. Mater. Chem. A* **2015**, *3*, 11750–11755.

[89] You, J. B.; Meng, L.; Song, T.-B.; Guo, T.-F.; Yang, Y. M.; Chang, W.-H.; Hong, Z. R.; Chen, H. J.; Zhou, H. P.; Chen, Q. et al. Improved air stability of perovskite solar cells via solution-processed metal oxide transport layers. *Nat. Nanotechnol.* **2016**, *11*, 75–81.

[90] Yang, G.; Tao, H.; Qin, P. L.; Ke, W. J.; Fang, G. J. Recent progress in electron transport layers for efficient perovskite solar cells. *J. Mater. Chem. A* **2016**, *4*, 3970–3990.

[91] Xia, F.; Wu, Q. L.; Zhou, P. C.; Li, Y.; Chen, X.; Liu, Q.; Zhu, J.; Dai, S. Y.; Lu, Y. L.; Yang, S. F. Efficiency enhancement of inverted structure perovskite solar cells via oleamide doping of PCBM electron transport layer. *ACS Appl. Mater. Interfaces* **2015**, *7*, 13659–13665.

[92] Chang, C.-Y.; Huang, W.-K.; Chang, Y.-C.; Lee, K.-T.; Chen, C.-T. A solution-processed n-doped fullerene cathode interfacial layer for efficient and stable large-area perovskite solar cells. *J. Mater. Chem. A* **2016**, *4*, 640–648.

[93] Bai, Y.; Yu, H.; Zhu, Z. L.; Jiang, K.; Zhang, T.; Zhao, N.; Yang, S. H.; Yan, H. High performance inverted structure perovskite solar cells based on a PCBM: Polystyrene blend electron transport layer. *J. Mater. Chem. A* **2015**, *3*, 9098–9102.

[94] Niu, G. D.; Guo, X. D.; Wang, L. D. Review of recent progress in chemical stability of perovskite solar cells. *J. Mater. Chem. A* **2015**, *3*, 5360–5367.

[95] Li, J. W.; Li, W. Z.; Dong, H. P.; Li, N.; Guo, X. D.; Wang, L. D. Enhanced performance in hybrid perovskite solar cell by modification with spinel lithium titanate. *J. Mater. Chem. A* **2015**, *3*, 8882–8889.

[96] Hawash, Z.; Ono, L. K.; Raga, S. R.; Lee, M. V.; Qi, Y. B. Air-exposure induced dopant redistribution and energy level shifts in spin-coated spiro-MeOTAD films. *Chem. Mater.* **2015**, *27*, 562–569.

[97] Jung, M.-C.; Raga, S. R.; Ono, L. K.; Qi, Y. B. Substantial improvement of perovskite solar cells stability by pinhole-free hole transport layer with doping engineering. *Sci. Rep.* **2015**, *5*, 9863.

[98] Shit, A.; Nandi, A. K. Interface engineering of hybrid perovskite solar cells with poly(3-thiophene acetic acid) under ambient conditions. *Phys. Chem. Chem. Phys.* **2016**, *18*, 10182–10190.

[99] Hou, Y.; Chen, W.; Baran, D.; Stubhan, T.; Luechinger, N. A.; Hartmeier, B.; Richter, M.; Min, J.; Chen, S.; Quiroz, C. O. R. et al. Overcoming the interface losses in planar heterojunction perovskite-based solar cells. *Adv. Mater.* **2016**, *28*, 5112–5120.

[100] Zhu, Z. L.; Bai, Y.; Lee, H. K. H.; Mu, C.; Zhang, T.; Zhang, L. X.; Wang, J. N.; Yan, H.; So, S. K.; Yang, S. H. Polyfluorene derivatives are high-performance organic hole-transporting materials for inorganic−organic hybrid perovskite solar cells. *Adv. Funct. Mater.* **2014**, *24*, 7357–7365.

[101] Liu, J.; Wu, Y. Z.; Qin, C. J.; Yang, X. D.; Yasuda, T.; Islam, A.; Zhang, K.; Peng, W. Q.; Chen, W.; Han, L. Y. A dopant-free hole-transporting material for efficient and stable perovskite solar cells. *Energy Environ. Sci.* **2014**, *7*, 2963–2967.

[102] Manders, J. R.; Tsang, S. W.; Hartel, M. J.; Lai, T. H.; Chen, S.; Amb, C. M.; Reynolds, J. R.; So, F. Solution-processed nickel oxide hole transport layers in high efficiency polymer photovoltaic cells. *Adv. Funct. Mater.* **2013**, *23*, 2993–3001.

[103] Seo, J.; Park, S.; Kim, Y. C.; Jeon, N. J.; Noh, J. H.; Yoon, S. C.; Seok, S. I. Benefits of very thin PCBM and LiF layers for solution-processed p–i–n perovskite solar cells. *Energy Environ. Sci.* **2014**, *7*, 2642–2646.

[104] Fu, Q. X.; Tang, X. L.; Tan, L. C.; Zhang, Y.; Liu, Y. W.; Chen, L.; Chen, Y. W. Versatile molybdenum isopropoxide for efficient mesoporous perovskite solar cells: Simultaneously optimized morphology and interfacial engineering. *J. Phys. Chem. C* **2016**, *120*, 15089–15095.

[105] Back, H.; Kim, G.; Kim, J.; Kong, J.; Kim, T. K.; Kang, H.; Kim, H.; Lee, J.; Lee, S.; Lee, K. Achieving long-term stable perovskite solar cells via ion neutralization. *Energy Environ. Sci.* **2016**, *9*, 1258–1263.

[106] Li, W. Z.; Zhang, W.; Van Reenen, S.; Sutton, R. J.; Fan, J. D.; Haghighirad, A. A.; Johnston, M. B.; Wang, L. D.; Snaith, H. J. Enhanced UV-light stability of planar heterojunction perovskite solar cells with caesium bromide interface modification. *Energy Environ. Sci.* **2016**, *9*, 490–498.

[107] Shi, J. J.; Dong, W.; Xu, Y.-Z.; Li, C.-H.; Lv, S.-T.; Zhu, L.-F.; Dong, J.; Luo, Y.-H.; Li, D.-M.; Meng, Q.-B. et al. Enhanced performance in perovskite organic lead iodide heterojunction solar cells with metal-insulator-semiconductor back contact. *Chin. Phys. Lett.* **2013**, *30*, 128402.

[108] Niu, G. D.; Li, W. Z.; Meng, F. Q.; Wang, L. D.; Dong, H. P.; Qiu, Y. Study on the stability of $CH_3NH_3PbI_3$ films and the effect of post-modification by aluminum oxide in all-solid-state hybrid solar cells. *J. Mater. Chem. A* **2014**, *2*, 705–710.

[109] Dong, X.; Fang, X.; Lv, M. H.; Lin, B. C.; Zhang, S.; Ding, J. N.; Yuan, N. Y. Improvement of the humidity stability of organic–inorganic perovskite solar cells using ultrathin Al_2O_3 layers prepared by atomic layer deposition. *J. Mater. Chem. A* **2015**, *3*, 5360–5367.

[110] Marin-Beloqui, J. M.; Lanzetta, L.; Palomares, E. Decreasing charge losses in perovskite solar cells through mp-TiO_2/MAPI interface engineering. *Chem. Mater.* **2016**, *28*, 207–213.

[111] Docampo, P.; Ball, J. M.; Darwich, M.; Eperon, G. E.; Snaith, H. J. Efficient organometal trihalide perovskite planar-heterojunction solar cells on flexible polymer substrates. *Nat. Commun.* **2013**, *4*, 2761.

[112] Bai, S.; Wu, Z. W.; Wu, X. J.; Jin, Y. Z.; Zhao, N.; Chen, Z. H.; Mei, Q. Q.; Wang, X.; Ye, Z. Z.; Song, T. et al. High-performance planar heterojunction perovskite solar cells: Preserving long charge carrier diffusion lengths and interfacial engineering. *Nano Res.* **2014**, *7*, 1749–1758.

[113] Guo, X. D.; Dong, H. P.; Li, W. Z.; Li, N.; Wang, L. D. Multifunctional MgO layer in perovskite solar cells. *ChemPhysChem* **2015**, *16*, 1727–1732.

[114] Ogomi, Y.; Kukihara, K.; Qing, S.; Toyoda, T.; Yoshino, K.; Pandey, S.; Momose, H.; Hayase, S. Control of charge dynamics through a charge-separation interface for all-solid perovskite-sensitized solar cells. *ChemPhysChem* **2014**, *15*, 1062–1069.

[115] Kaltenbrunner, M.; Adam, G.; Głowacki, E. D.; Drack, M.; Schwödiauer, R.; Leonat, L.; Apaydin, D. H.; Groiss, H.; Scharber, M. C.; White, M. S. et al. Flexible high power-per-weight perovskite solar cells with chromium oxide-metal contacts for improved stability in air. *Nat. Mater.* **2015**, *14*, 1032–1039.

[116] Domanski, K.; Correa-Baena, J.-P.; Mine, N.; Nazeeruddin, M. K.; Abate, A.; Saliba, M.; Tress, W.; Hagfeldt, A.; Grätzel, M. Not all that glitters is gold: Metal-migration-induced degradation in perovskite solar cells. *ACS Nano* **2016**, *10*, 6306–6314.

[117] Dong, H. P.; Guo, X. D.; Li, W. Z.; Wang, L. D. Cesium carbonate as a surface modification material for organic–inorganic hybrid perovskite solar cells with enhanced performance. *RSC Adv.* **2014**, *4*, 60131–60134.

[118] Hu, Q.; Wu, J.; Jiang, C.; Liu, T. H.; Que, X. L.; Zhu, R.; Gong, Q. H. Engineering of electron-selective contact for perovskite solar cells with efficiency exceeding 15%. *ACS Nano* **2014**, *8*, 10161–10167.

[119] Ito, S.; Tanaka, S.; Manabe, K.; Nishino, H. Effects of surface blocking layer of Sb_2S_3 on nanocrystalline TiO_2 for $CH_3NH_3PbI_3$ perovskite solar cells. *J. Phys. Chem. C* **2014**, *118*, 16995–17000.

[120] Tress, W.; Marinova, N.; Moehl, T.; Zakeeruddin, S. M.; Nazeeruddin, M. K.; Grätzel, M. Understanding the rate-dependent *J–V* hysteresis, slow time component, and aging in $CH_3NH_3PbI_3$ perovskite solar cells: The role of a compensated electric field. *Energy Environ. Sci.* **2015**, *8*, 995–1004.

[121] Xiao, Z. G.; Yuan, Y. B.; Shao, Y. C.; Wang, Q.; Dong, Q. F.; Bi, C.; Sharma, P.; Gruverman, A.; Huang, J. S. Giant switchable photovoltaic effect in organometal trihalide perovskite devices. *Nat. Mater.* **2015**, *14*, 193–198.

[122] Shao, Y. C.; Xiao, Z. G.; Bi, C.; Yuan, Y. B.; Huang, J. S. Origin and elimination of photocurrent hysteresis by fullerene passivation in $CH_3NH_3PbI_3$ planar heterojunction solar cells. *Nat. Commun.* **2014**, *5*, 5784.

[123] Wu, Y. Z.; Chen, W.; Yue, Y. F.; Liu, J.; Bi, E. B.; Yang, X. D.; Islam, A.; Han, L. Y. Consecutive morphology controlling operations for highly reproducible mesostructured perovskite solar cells. *ACS Appl. Mater. Interfaces* **2015**, *7*, 20707–20713.

[124] Azimi, H.; Ameri, T.; Zhang, H.; Hou, Y.; Quiroz, C. O. R.; Min, J.; Hu, M. Y.; Zhang, Z. G.; Przybilla, T.; Matt, G. J. et al. A universal interface layer based on an amine-functionalized fullerene derivative with dual functionality for efficient solution processed organic and perovskite solar cells. *Adv. Energy Mater.* **2015**, *5*, 1401692.

[125] Liu, Y.; Bag, M.; Renna, L. A.; Page, Z. A.; Kim, P.; Emrick, T.; Venkataraman, D.; Russell, T. P. Understanding interface engineering for high-performance fullerene/perovskite planar heterojunction solar cells. *Adv. Energy Mater.* **2016**, *6*, 1501606.

[126] Wojciechowski, K.; Stranks, S. D.; Abate, A.; Sadoughi, G.; Sadhanala, A.; Kopidakis, N.; Rumbles, G.; Li, C.-Z.; Friend, R. H.; Jen, A. K.-Y. Heterojunction modification for highly efficient organic–inorganic perovskite solar cells. *ACS Nano* **2014**, *8*, 12701–12709.

[127] Li, Y. W.; Zhao, Y.; Chen, Q.; Yang, Y.; Liu, Y. S.; Hong, Z. R.; Liu, Z. H.; Hsieh, Y.-T.; Meng, L.; Li, Y. F. et al. Multifunctional fullerene derivative for interface engineering in perovskite solar cells. *J. Am. Chem. Soc.* **2015**, *137*, 15540–15547.

[128] Li, W. Z.; Dong, H. P.; Guo, X. D.; Li, N.; Li, J. W.; Niu, G. D.; Wang, L. D. Graphene oxide as dual functional interface modifier for improving wettability and retarding recombination in hybrid perovskite solar cells. *J. Mater. Chem. A* **2014**, *2*, 20105–20111.

[129] Agresti, A.; Pescetelli, S.; Cinà, L.; Konios, D.; Kakavelakis, G.; Kymakis, E.; Di Carlo, A. Efficiency and stability enhancement in perovskite solar cells by inserting lithium-neutralized graphene oxide as electron transporting layer. *Adv. Funct. Mater.* **2016**, *26*, 2686–2694.

[130] Feng, S. L.; Yang, Y. G.; Li, M.; Wang, J. M.; Cheng, Z. D.; Li, J. H.; Ji, G. W.; Yin, G. Z.; Song, F.; Wang, Z.-K. et al. High-performance perovskite solar cells engineered by an ammonia modified graphene oxide interfacial layer. *ACS Appl. Mater. Interfaces* **2016**, *8*, 14503–14512.

[131] Habisreutinger, S. N.; Leijtens, T.; Eperon, G. E.; Stranks, S. D.; Nicholas, R. J.; Snaith, H. J. Carbon nanotube/polymer composites as a highly stable hole collection layer in perovskite solar cells. *Nano Lett.* **2014**, *14*, 5561–5568.

[132] Habisreutinger, S. N.; Leijtens, T.; Eperon, G. E.; Stranks, S. D.; Nicholas, R. J.; Snaith, H. J. Enhanced hole extraction in perovskite solar cells through carbon nanotubes. *J. Phys. Chem. Lett.* **2014**, *5*, 4207–4212.

[133] Li, Z.; Kulkarni, S. A.; Boix, P. P.; Shi, E. Z.; Cao, A. Y.; Fu, K. W.; Batabyal, S. K.; Zhang, J.; Xiong, Q. H.; Wong, L. H. et al. Laminated carbon nanotube networks for metal electrode-free efficient perovskite solar cells. *ACS Nano* **2014**, *8*, 6797–6804.

[134] Zuo, L. J.; Gu, Z. W.; Ye, T.; Fu, W. F.; Wu, G.; Li, H. Y.; Chen, H. Z. Enhanced photovoltaic performance of $CH_3NH_3PbI_3$ perovskite solar cells through interfacial engineering using self-assembling monolayer. *J. Am. Chem. Soc.* **2015**, *137*, 2674–2679.

[135] Liu, L. F.; Mei, A. Y.; Liu, T. F.; Jiang, P.; Sheng, Y. S.; Zhang, L. J.; Han, H. W. Fully printable mesoscopic perovskite solar cells with organic silane self-assembled monolayer. *J. Am. Chem. Soc.* **2015**, *137*, 1790–1793.

[136] Ogomi, Y.; Morita, A.; Tsukamoto, S.; Saitho, T.; Shen, Q.; Toyoda, T.; Yoshino, K.; Pandey, S. S.; Ma, T. L.; Hayase, S. All-solid perovskite solar cells with HOCO–R–$NH^{3+}I^-$ anchor-group inserted between porous titania and perovskite. *J. Phys. Chem. C* **2014**, *118*, 16651–16659.

[137] Shih, Y. C.; Wang, L. Y.; Hsieh, H. C.; Lin, K. F. Enhancing the photocurrent of perovskite solar cells via modification of the $TiO_2/CH_3NH_3PbI_3$ heterojunction interface with amino acid. *J. Mater. Chem. A* **2015**, *3*, 9133–9136.

[138] Cao, J.; Yin, J.; Yuan, S. F.; Zhao, Y.; Li, J.; Zheng, N. F. Thiols as interfacial modifiers to enhance the performance and stability of perovskite solar cells. *Nanoscale* **2015**, *7*, 9443–9447.

[139] Yang, S.; Wang, Y.; Liu, P. R.; Cheng, Y.-B.; Zhao, H. J.; Yang, H. G. Functionalization of perovskite thin films with moisture-tolerant molecules. *Nat. Energy* **2016**, *1*, 15016.

[140] Zhang, J.; Hu, Z. L.; Huang, L. K.; Yue, G. Q.; Liu, J. W.; Lu, X. W.; Hu, Z. Y.; Shang, M. H.; Han, L. Y.; Zhu, Y. J. Bifunctional alkyl chain barriers for efficient perovskite solar cells. *Chem. Commun.* **2015**, *51*, 7047–7050.

[141] Chiang, C.-H.; Tseng, Z.-L.; Wu, C.-G. Planar heterojunction perovskite/$PC_{71}BM$ solar cells with enhanced open-circuit voltage via a (2/1)-step spin-coating process. *J. Mater. Chem. A* **2014**, *2*, 15897–15903.

[142] Jeng, J. Y.; Chiang, Y. F.; Lee, M. H.; Peng, S. R.; Guo, T. F.; Chen, P.; Wen, T. C. $CH_3NH_3PbI_3$ perovskite/fullerene planar-heterojunction hybrid solar cells. *Adv. Mater.* **2013**, *25*, 3727–3732.

[143] Wang, Q.; Shao, Y. C.; Dong, Q. F.; Xiao, Z. G.; Yuan, Y. B.; Huang, J. S. Large fill-factor bilayer iodine perovskite solar cells fabricated by a low-temperature solution-process. *Energy Environ. Sci.* **2014**, *7*, 2359–2365.

[144] Min, J.; Zhang, Z.-G.; Hou, Y.; Ramirez Quiroz, C. O.; Przybilla, T.; Bronnbauer, C.; Guo, F.; Forberich, K.; Azimi, H.; Ameri, T. et al. Interface engineering of perovskite hybrid solar cells with solution-processed perylene–diimide heterojunctions toward high performance. *Chem. Mater.* **2015**, *27*, 227–234.

[145] Qian, M.; Li, M.; Shi, X.-B.; Ma, H.; Wang, Z.-K.; Liao, L.-S. Planar perovskite solar cells with 15.75% power conversion efficiency by cathode and anode interfacial modification. *J. Mater. Chem. A* **2015**, *3*, 13533–13539.

[146] Sun, K.; Chang, J. J.; Isikgor, F. H.; Li, P. C.; Ouyang, J. Y. Efficiency enhancement of planar perovskite solar cells by adding zwitterion/LiF double interlayers for electron collection. *Nanoscale* **2015**, *7*, 896–900.

[147] Jiang, L.-L.; Cong, S.; Lou, Y.-H.; Yi, Q.-H.; Zhu, J.-T.; Ma, H.; Zou, G.-F. Interface engineering toward enhanced efficiency of planar perovskite solar cells. *J. Mater. Chem. A* **2016**, *4*, 217–222.

[148] Yuan, D.-X.; Yuan, X.-D.; Xu, Q.-Y.; Xu, M.-F.; Shi, X.-B.; Wang, Z.-K.; Liao, L.-S. A solution-processed bathocuproine cathode interfacial layer for high-performance bromine–iodine perovskite solar cells. *Phys. Chem. Chem. Phys.* **2015**, *17*, 26653–26658.

[149] Li, C.; Wang, F. Z.; Xu, J.; Yao, J. X.; Zhang, B.; Zhang, C. F.; Xiao, M.; Dai, S. Y.; Li, Y. F.; Tan, Z. A. Efficient perovskite/fullerene planar heterojunction solar cells with enhanced charge extraction and suppressed charge recombination. *Nanoscale* **2015**, *7*, 9771–9778.

[150] Zhang, H.; Azimi, H.; Hou, Y.; Ameri, T.; Przybilla, T.; Spiecker, E.; Kraft, M.; Scherf, U.; Brabec, C. J. Improved high-efficiency perovskite planar heterojunction solar cells via incorporation of a polyelectrolyte interlayer. *Chem. Mater.* **2014**, *26*, 5190–5193.

[151] Xue, Q. F.; Hu, Z. C.; Liu, J.; Lin, J. H.; Sun, C.; Chen, Z. M.; Duan, C. H.; Wang, J.; Liao, C.; Lau, W. M. et al. Highly efficient fullerene/perovskite planar heterojunction solar cells via cathode modification with an amino-functionalized polymer interlayer. *J. Mater. Chem. A* **2014**, *2*, 19598–19603.

[152] Chen, W.; Zhu, Y. D.; Yu, Y. Z.; Xu, L. M.; Zhang, G. N.; He, Z. B. Low cost and solution processed interfacial layer based on poly(2-ethyl-2-oxazoline) nanodots for inverted perovskite solar cells. *Chem. Mater.* **2016**, *28*, 4879–4883.

[153] Wang, K.; Liu, C.; Yi, C.; Chen, L.; Zhu, J. H.; Weiss, R. A.; Gong, X. Efficient perovskite hybrid solar cells via ionomer interfacial engineering. *Adv. Funct. Mater.* **2015**, *25*, 6875–6884.

[154] Wang, Q.; Dong, Q. F.; Li, T.; Gruverman, A.; Huang, J. S. Thin insulating tunneling contacts for efficient and water-resistant perovskite solar cells. *Adv. Mater.* **2016**, *28*, 6734–6739.

[155] Zhu, Z. L.; Ma, J. N.; Wang, Z. L.; Mu, C.; Fan, Z. T.; Du, L. L.; Bai, Y.; Fan, L. Z.; Yan, H.; Phillips, D. L. et al. Efficiency enhancement of perovskite solar cells through fast electron extraction: The role of graphene quantum dots. *J. Am. Chem. Soc.* **2014**, *136*, 3760–3763.

[156] Tavakoli, M. M.; Tavakoli, R.; Nourbakhsh, Z.; Waleed, A.; Virk, U. S.; Fan, Z. Y. High efficiency and stable perovskite solar cell using ZnO/rGO QDs as an electron transfer layer. *Adv. Mater. Interfaces* **2016**, *3*, 1500790.

[157] Cha, M. Y.; Da, P. M.; Wang, J.; Wang, W. Y.; Chen, Z. H.; Xiu, F. X.; Zheng, G. F.; Wang, Z.-S. Enhancing perovskite solar cell performance by interface engineering using $CH_3NH_3PbBr_{0.9}I_{2.1}$ quantum dots. *J. Am. Chem. Soc.* **2016**, *138*, 8581–8587.

[158] Hu, L.; Wang, W. W.; Liu, H.; Peng, J.; Cao, H. F.; Shao, G.; Xia, Z.; Ma, W. L.; Tang, J. PbS colloidal quantum dots as an effective hole transporter for planar heterojunction perovskite solar cells. *J. Mater. Chem. A* **2015**, *3*, 515–518.

[159] Li, Y.; Zhu, J.; Huang, Y.; Wei, J. F.; Liu, F.; Shao, Z. P.; Hu, L. H.; Chen, S. H.; Yang, S. F.; Tang, J. W. et al. Efficient inorganic solid solar cells composed of perovskite and PbS quantum dots. *Nanoscale* **2015**, *7*, 9902–9907.

[160] Zhang, F.; Zhong, H. Z.; Chen, C.; Wu, X.-G.; Hu, X. M.; Huang, H. L.; Han, J. B.; Zou, B. S.; Dong, Y. P. Brightly luminescent and color-tunable colloidal $CH_3NH_3PbX_3$ (X = Br, I, Cl) quantum dots: Potential alternatives for display technology. *ACS Nano* **2015**, *9*, 4533–4542.

[161] Wei, H. Y.; Shi, J. J.; Xu, X.; Xiao, J. Y.; Luo, J. H.; Dong, J.; Lv, S. T.; Zhu, L. F.; Wu, H. J.; Li, D. M. et al. Enhanced charge collection with ultrathin AlO_x electron blocking layer for hole-transporting material-free perovskite solar cell. *Phys. Chem. Chem. Phys.* **2015**, *17*, 4937–4944.

[162] Dong, J.; Zhao, Y. H.; Shi, J. J.; Wei, H. Y.; Xiao, J. Y.; Xu, X.; Luo, J. H.; Xu, J.; Li, D. M.; Luo, Y. H. et al. Impressive enhancement in the cell performance of ZnO nanorod-based perovskite solar cells with Al-doped ZnO interfacial modification. *Chem. Commun.* **2014**, *50*, 13381–13384.

[163] Wang, Z.-K.; Li, M.; Yuan, D.-X.; Shi, X.-B.; Ma, H.; Liao, L.-S. Improved hole interfacial layer for planar perovskite solar cells with efficiency exceeding 15%. *ACS Appl. Mater. Interfaces* **2015**, *7*, 9645–9651.

[164] Han, G. S.; Chung, H. S.; Kim, B. J.; Kim, D. H.; Lee, J. W.; Swain, B. S.; Mahmood, K.; Yoo, J. S.; Park, N.-G.; Lee, J. H. et al. Retarding charge recombination in perovskite solar cells using ultrathin MgO-coated TiO_2 nanoparticulate films. *J. Mater. Chem. A* **2015**, *3*, 9160–9164.

[165] Kim, J.; Kim, G.; Kim, T. K.; Kwon, S.; Back, H.; Lee, J.; Lee, S. H.; Kang, H.; Lee, K. Efficient planar-heterojunction perovskite solar cells achieved via interfacial modification of a sol–gel ZnO electron collection layer. *J. Mater. Chem. A* **2014**, *2*, 17291–17296.

[166] Tao, C.; Neutzner, S.; Colella, L.; Marras, S.; Kandada, A. R. S.; Gandini, M.; De Bastiani, M.; Pace, G.; Manna, L.; Caironi, M. et al. 17.6% stabilized efficiency in low-temperature processed planar perovskite solar cells. *Energy Environ. Sci.* **2015**, *8*, 2365–2370.

[167] Dong, Y.; Li, W. H.; Zhang, X. J.; Xu, Q.; Liu, Q.; Li, C. H.; Bo, Z. S. Highly efficient planar perovskite solar cells via interfacial modification with fullerene derivatives. *Small* **2016**, *12*, 1098–1104.

[168] Ihly, R.; Dowgiallo, A.-M.; Yang, M. J.; Schulz, P.; Stanton, N. J.; Reid, O. G.; Ferguson, A. J.; Zhu, K.; Berry, J. J.; Blackburn, J. L. Efficient charge extraction and slow recombination in organic–inorganic perovskites capped with semiconducting single-walled carbon nanotubes. *Energy Environ. Sci.* **2016**, *9*, 1439–1449.

[169] Tavakoli, M. M.; Tavakoli, R.; Hasanzadeh, S.; Mirfasih, M. H. Interface engineering of perovskite solar cell using a reduced-graphene scaffold. *J. Phys. Chem. C* **2016**, *120*, 19531–19536.

[170] Abate, A.; Saliba, M.; Hollman, D. J.; Stranks, S. D.; Wojciechowski, K.; Avolio, R.; Grancini, G.; Petrozza, A.; Snaith, H. J. Supramolecular halogen bond passivation of organic–inorganic halide perovskite solar cells. *Nano Lett.* **2014**, *14*, 3247–3254.

[171] Chang, C.-Y.; Chang, Y.-C.; Huang, W.-K.; Lee, K.-T.; Cho, A.-C.; Hsu, C.-C. Enhanced performance and stability of semitransparent perovskite solar cells using solution-processed thiol-functionalized cationic surfactant as cathode buffer layer. *Chem. Mater.* **2015**, *27*, 7119–7127.

[172] Zhang, J.; Wang, P.; Huang, X. K.; Xu, J.; Wang, L. M.; Yue, G. Q.; Lu, X. W.; Liu, J. W.; Hu, Z. Y.; Wang, Q. et al. Polar molecules modify perovskite surface to reduce recombination in perovskite solar cells. *RSC Adv.* **2016**, *6*, 9090–9095.

[173] Bai, Y.; Chen, H. N.; Xiao, S.; Xue, Q. F.; Zhang, T.; Zhu, Z. L.; Li, Q.; Hu, C.; Yang, Y.; Hu, Z. C. et al. Effects of a molecular monolayer modification of NiO nanocrystal layer surfaces on perovskite crystallization and interface contact toward faster hole extraction and higher photovoltaic performance. *Adv. Funct. Mater.* **2016**, *26*, 2950–2958.

[174] Xu, Y. Z.; Shi, J. J.; Lv, S. T.; Zhu, L. F.; Dong, J.; Wu, H. J.; Xiao, Y.; Luo, Y. H.; Wang, S. R.; Li, D. M. et al. Simple way to engineer metal–semiconductor interface for enhanced performance of perovskite organic lead iodide solar cells. *ACS Appl. Mater. Interfaces* **2014**, *6*, 5651–5656.

[175] Hu, Q.; Liu, Y.; Li, Y.; Ying, L.; Liu, T. H.; Huang, F.; Wang, S. F.; Huang, W.; Zhu, R.; Gong, Q. H. Efficient and low-temperature processed perovskite solar cells based on a cross-linkable hybrid interlayer. *J. Mater. Chem. A* **2015**, *3*, 18483–18491.

[176] Dong, H. P.; Li, Y.; Wang, S. F.; Li, W. Z.; Li, N.; Guo, X. D.; Wang, L. D. Interface engineering of perovskite solar cells with PEO for improved performance. *J. Mater. Chem. A* **2015**, *3*, 9999–10004.

[177] Yun, J. H.; Lee, I.; Kim, T.-S.; Ko, M. J.; Kim, J. Y.; Son, H. J. Synergistic enhancement and mechanism study of mechanical and moisture stability of perovskite solar cells introducing polyethylene-imine into the $CH_3NH_3PbI_3$/HTM interface. *J. Mater. Chem. A* **2015**, *3*, 22176–22182.

[178] Da, P. M.; Cha, M. Y.; Sun, L.; Wu, Y. Z.; Wang, Z.-S.; Zheng, G. F. High-performance perovskite photoanode enabled by Ni passivation and catalysis. *Nano Lett.* **2015**, *15*, 3452–3457.

[179] Crespo-Quesada, M.; Pazos-Outón, L. M.; Warnan, J.; Kuehnel, M. F.; Friend, R. H.; Reisner, E. Metal-encapsulated organolead halide perovskite photocathode for solar-driven hydrogen evolution in water. *Nat. Commun.* **2016**, *7*, 12555.

[180] Hoang, M. T.; Pham, N. D.; Han, J. H.; Gardner, J. M.; Oh, I. Integrated photoelectrolysis of water implemented on organic metal halide perovskite photoelectrode. *ACS Appl. Mater. Interfaces* **2016**, *8*, 11904–11909.